Applied Acoustics 257 (2027) 111567

Contents lists available at ScienceDirect

Applied Acoustics

journal homepage: www.elsevier.com/locate/apacoust

Sensitivity-guided modeling of exhaust noise in large-bore marine engines using 1D acoustic simulation

Touraj Hashempour [a,*], Jeyoung Kim [a], Muhammad Danish Idrees [a], Carlo Pestelli [b], Zengxin Gao [b], Maciej Mikulski [a]

[a] Efficient Powertrain Solutions (EPS), School of Technology and Innovations, University of Vaasa, Yliopistonranta 10, FI-65200 Vaasa, Finland
[b] Wärtsilä Finland Oy, Vaasa, Finland

ARTICLE INFO

Keywords:
Exhaust noise
Acoustic simulation
One-dimensional model
Large-bore engine
Medium-speed engine
Marine engine

ABSTRACT

Accurate prediction of exhaust noise is increasingly important for integrating acoustic constraints into model-based development of large-bore marine engines. However, one-dimensional acoustic modeling practices established primarily for automotive engines may not transfer directly to large-bore systems. This study investigates the sensitivity of predicted exhaust-pressure spectra to numerical resolution, downstream exhaust-stack representation, turbocharger acoustic modeling, and local duct geometry using a one-dimensional model of a Wärtsilä 4L20 medium-speed engine. A configuration combining the selected refinements is then evaluated against measured in-duct pressure spectra. Numerical resolution produced the strongest sensitivity, with coupled spatial–temporal refinement reducing the spectral RMSE relative to the finest-mesh reference from 10.7 to 2.3 dB below 600 Hz. Explicit exhaust-stack representation substantially redistributed spectral energy, while an acoustic turbine representation introduced frequency-dependent transmission loss rising to 15–17 dB near 1 kHz. The combined refined configuration produced closer frequency-resolved agreement immediately downstream of the turbine, where the narrowband RMSE decreased from 11.42 to 9.88 dB and the mean absolute error from 9.66 to 7.57 dB, although the mean-level deviation increased from 2.42 to 3.05 dB. Within the plane-wave-valid range, one-third-octave errors also decreased, and a separate comparison at a farther-downstream station gave a mean absolute error of 7.30 dB, although residual narrowband discrepancies of 9–10 dB remained. The results demonstrate that reliable one-dimensional exhaust-acoustic prediction for the investigated large-bore engine requires adequate numerical wave resolution together with representation of the dominant propagation paths and passive turbine acoustics. However, the remaining spectral errors indicate that further model development and validation are required. The quantitative resolution thresholds and relative importance of individual model components remain platform-specific and require validation across additional engines and operating conditions.

1. Introduction

Noise-control requirements for marine and stationary power systems arise from several regulatory frameworks. These include Directive 2000/14/EC for specified outdoor equipment and Directive 2002/49/EC for environmental-noise assessment and management [1,2], while the International Maritime Organization has issued guidelines for underwater radiated noise from shipping [3] and a Code on Noise Levels on Board Ships that limits crew and passenger exposure [4]. Although these instruments do not define a single exhaust-noise limit for the investigated engine, they establish a broader design context in which early acoustic prediction can reduce reliance on costly retrofit measures.

Exhaust noise is typically the dominant excitation in internal combustion engines and is particularly significant in large-bore marine and stationary units [5,6]. These systems pose acoustic challenges that differ qualitatively from those of smaller automotive engines. Large cylinder displacement produces high-amplitude exhaust-pressure pulsations, and operation at approximately 400–1000 rpm concentrates the dominant acoustic energy at low firing-frequency harmonics, commonly below about 250 Hz, where attenuation is considerably harder than for the mid-frequency content typical of automotive engines [6]. Long and geometrically complex exhaust paths introduce multiple partial reflections at area discontinuities and junctions, substantial phase accumulation along each segment, and spatially varying sound speed caused

* Corresponding author.
E-mail address: touraj.hashempour@uwasa.fi (T. Hashempour).

https://doi.org/10.1016/j.apacoust.2026.111567
Received 19 May 2026; Received in revised form 11 September 2026; Accepted 14 September 2026

by axial and wall-to-gas temperature gradients. Large duct diameters lower the cut-on frequency of the first transverse mode and therefore restrict the frequency range over which a plane-wave model is valid, while the hot, non-uniform gas temperature modifies the acoustic wavelength and phase propagation [7]. Consequently, the observed low-frequency spectrum is governed by the complete exhaust path rather than by any single component. Installation constraints on ships and stationary power plants additionally limit the use of compact reactive mufflers, generally requiring large multi-stage silencers or expansion chambers [6,8]. Comparable sensitivity of low-frequency response to forcing frequency, sound-pressure level, and medium properties has been observed in other acoustically driven media [9,10], supporting the need to validate spectral predictions in the actual exhaust environment.

Engine modifications that may alter noise emissions generally require experimental verification, while performance calibration and acoustic validation are often conducted as separate development stages [11]. This separation is becoming increasingly costly as the design space of modern engines expands. Low-carbon marine engine concepts including hydrogen-enriched dual-fuel operation and Reactivity Controlled Compression Ignition (RCCI) substantially widen the calibration space compared with conventional diesel combustion [12,13]. Multi-zone thermo-kinetic combustion models illustrate the strong coupling among the underlying combustion processes [14]. These conditions motivate the early integration of acoustic constraints into system-level virtual development [15], particularly because much existing engine-acoustics knowledge originates from automotive applications [16].

High-fidelity three-dimensional (3D) methods resolve non-planar propagation, complex junction effects, and flow–acoustic coupling that lie beyond the reach of one-dimensional (1D) networks. Applications range from turbocharger compressor and intake-duct acoustics, where broadband spectra are derived from transient pressure records [17], to complex exhaust flow-noise using compressible 3D-CFD direct-noise workflows that typically require hundreds of CPU-hours per operating point [18], and CFD–FEM couplings that predict the transmission loss of marine after-treatment components at substantially lower cost than fully transient CFD [19]. Even so, the model-preparation effort and computational demand of 3D approaches restrict their practical use in system-level parametric studies covering many layouts and operating points. One-dimensional acoustic network models, by contrast, resolve wave propagation along the main flow path with much lower cost and are widely used for rapid screening, calibration workflows, and iterative design studies, with higher-dimensional or hybrid approaches reserved for components where non-planar propagation or higher-order modes must be captured [20].

Prior 1D acoustic work on engine exhaust systems has evolved along two directions. One line combines 1D time-domain models of the engine and duct network with a 3D frequency-domain treatment of geometrically complex silencing elements, delivering close agreement with experiments at moderate cost [21,22]; comparable 1D–3D exhaust-manifold analyses have shown that geometric tuning effectively attenuates pulsations and that 1D modeling is a practical predictor when experimentally validated [23]. A parallel line refines the 1D formulation itself: detailed correlation studies against chassis-dyno measurements have shown that accurate thermal representation of the duct system, and specifically the wall-heat-loss profile, is as important as the discretization of complex components for low-frequency acoustic prediction [7].

The accuracy of 1D unsteady wave propagation depends on coupled spatial and temporal resolution. A commonly used engineering criterion is to resolve the characteristic acoustic wavelength with at least approximately ten cells ($dX \leq \lambda/10$), although the resolution required to control numerical dispersion and phase error also depends on the numerical scheme and time step [24]. Applied to combustion engines, this criterion is commonly implemented by scaling the discretization length to a fraction of the cylinder bore: a factor of about 0.55 for exhaust and 0.4 for intake systems is typically adopted for performance-oriented explicit simulations, with roughly half of these values used when acoustic behavior is the priority [25]. These guidelines have been widely applied in 1D engine-modeling practice; however, they are based primarily on automotive-engine studies, and their extension to the substantially larger duct diameters, lower firing frequencies, and stronger thermal gradients of large-bore engines has not been systematically examined.

A second modeling axis on which 1D exhaust-acoustic prediction depends is the treatment of the turbocharger, since a substantial share of the low-frequency energy reaching the downstream duct network is shaped by the turbine's passive reflection and transmission behavior [26]. Recent work using fast 1D approaches has advanced the treatment of the compressor and turbine as elements with frequency-dependent acoustic transmission and reflection, rather than as steady-flow devices represented only by performance maps. Torregrosa et al. [27] characterized the turbine via operating-point-dependent transfer matrices generated from validated 1D simulations, enabling reflection and transmission behavior to be queried during engine simulation with limited additional computational cost. Veloso et al. [28] developed a geometry-based time-domain 1D gas-dynamics model of both compressor and turbine and reported consistent agreement with measured transmission loss up to 1600 Hz in both propagation directions. De Bellis et al. [29] combined dedicated steady/unsteady testing with a refined 1D turbine decomposition and showed that coupling a wheel-map with properly dimensioned internal pipes improves the predicted unsteady pressure and flow oscillations relative to a purely map-based turbine.

Despite these advances, the available 1D acoustic work remains focused on automotive or small-bore engines, and the assumptions and calibrated parameters embedded in existing practice do not straightforwardly transfer to the large-bore case. In particular, the discretization requirements, the acoustic role of the turbine, and the sensitivity of the predicted spectrum to duct-network geometry may all shift relative to automotive experience. Although 1D and hybrid methods have been shown to improve acoustic prediction and support component-level optimization, a clear gap remains for a systematic assessment of these effects in a large-bore engine, within a consistent one-dimensional time-domain framework that couples engine performance with exhaust-wave propagation.

The present study investigates how numerical resolution and physical representation of the exhaust flow path affect the one-dimensional prediction of unsteady pressure waves in a large-bore medium-speed engine. The examined factors comprise exhaust-domain discretization, explicit representation of the downstream duct network, passive turbine transmission, and local variations in duct and junction geometry. Their effects are interpreted through the coupled spatial and temporal resolution of the numerical solution, impedance discontinuities and phase accumulation within the duct network, distributed attenuation, and the passive transmission characteristics of the turbine. A configuration incorporating the physically supported refinements is subsequently evaluated against in-duct measurements within the plane-wave-valid frequency range. The study thereby provides a physics-based assessment of the requirements and limitations of one-dimensional exhaust-acoustic modeling for the investigated engine system.

Accordingly, the objectives are: (i) to quantify the sensitivity of the predicted pressure spectra to these four modeling factors; (ii) to interpret the observed sensitivities using the governing numerical and acoustic mechanisms; and (iii) to determine whether a configuration combining the physically supported refinements reduces the frequency-resolved discrepancies relative to measured in-duct spectra. The analysis distinguishes the general requirements of one-dimensional wave modeling from quantitative thresholds and component sensitivities that may depend on the engine geometry and operating condition.

2. Methodology

The study combines controlled numerical sensitivity analyses with in-duct pressure measurements. A performance-calibrated one-dimensional engine model provides the mean thermodynamic state and periodic exhaust excitation. The exhaust-domain resolution and representation of the principal wave-bearing components are then systematically varied, while the operating condition and the remaining numerical and physical assumptions are held fixed. This procedure isolates their influence on wave propagation, reflection, transmission, and attenuation. Finally, a configuration incorporating the identified refinements is evaluated against measured in-duct pressure spectra at the matched validation condition.

2.1. Experimental engine and acoustic measurements

The experiments were conducted on a four-cylinder Wärtsilä 4L20 medium-speed diesel research engine rated at approximately 0.8 MW and equipped with a single-stage turbocharger. The engine was operated at its nominal speed of 1000 rpm, which determines the fundamental rotational and firing frequencies relevant to the acoustic analysis. The engine specifications directly relevant to the present study are summarized in Table 1, while the intake- and exhaust-side pressure and temperature measurement locations are shown in Fig. 1.

Cycle-resolved in-cylinder, intake-port, and exhaust-port pressures were acquired over 87 consecutive engine cycles using the transducers listed in Table 2. The raw pressure channels were sampled at 100 kHz. For cycle-domain analysis, they were synchronized with the optical encoder and mapped to a 0.1° CA crank-angle grid. These measurements characterized the periodic exhaust excitation, supported derivation of the combustion input for the one-dimensional model, and related cylinder-pressure events to pressure-wave propagation across the turbine. Mean intake- and exhaust-side pressures and temperatures were additionally used to define and verify the simulated operating condition.

Fast-response Kistler 4049B transducers were installed immediately upstream and downstream of the turbine, while GRAS 40SC probe microphones were installed at the three downstream measurement ports shown in Figs. 2 and 3. The microphone measurements obtained at 1000 rpm and 400 kW provided the in-duct pressure spectra used for model validation. All acoustic channels were sampled at 100 kHz with anti-alias filtering, providing ample sampling bandwidth for the investigated range of 0–1000 Hz while remaining well below the Nyquist frequency.

2.2. Governing equations and baseline one-dimensional model

The baseline model was formulated to resolve the coupled mean-flow and pressure-wave dynamics that link the cylinder processes to the intake and exhaust systems. Over the frequency range of interest, each flow passage is represented as a cross-sectionally averaged duct, so the model resolves axial convection and pressure-wave propagation but not transverse variations within a section. Under this quasi-one-dimensional assumption, the unsteady compressible flow in a duct of variable cross-sectional area A is governed by the conservation equations for mass, axial momentum, and total energy given in Eq. (1) [24]:

$$\frac{\partial}{\partial t}\begin{bmatrix}\rho A\\ \rho uA\\ \rho EA\end{bmatrix}+\frac{\partial}{\partial x}\begin{bmatrix}\rho uA\\ (\rho u^2+p)A\\ u(\rho E+p)A\end{bmatrix}=\begin{bmatrix}0\\ p\dfrac{\partial A}{\partial x}\\ 0\end{bmatrix}+\boldsymbol{S}_{\mathrm{w}} \tag{1}$$

where ρ, u, p, and $E = e + u^2/2$ are the local gas density, axial velocity, static pressure, and specific total energy, with e the specific internal energy. The vector $\boldsymbol{S}_{\mathrm{w}}$ carries the distributed contributions of wall friction and gas–wall heat transfer. Where gas composition was tracked, the system was supplemented by separate species-continuity equations. Coupling with cylinders, valves, flow restrictions, and boundary elements enters through the interface fluxes and boundary conditions of the connected flow network.

Equation (1) retains the full nonlinear compressible formulation and can therefore represent finite-amplitude wave propagation, wave steepening, and weak shock formation near the turbine outlet at high load, while its small-perturbation limit recovers linear duct acoustics. When the pressure perturbation p' is small compared with the mean pressure, Eq. (1) reduces, in a duct of constant cross-section and in the absence of mean flow and losses, to the classical one-dimensional wave equation, Eq. (2):

$$\frac{\partial^2 p'}{\partial t^2}-c^2\frac{\partial^2 p'}{\partial x^2}=0 \tag{2}$$

with $c=\sqrt{\gamma RT}$ the local speed of sound at the prevailing gas temperature [30]. In the plane-wave regime, acoustic perturbations propagate predominantly as longitudinal waves along the duct axis. Their interaction with the duct network is governed by the characteristic acoustic impedance referenced to acoustic volume velocity, $Z_{\mathrm{c}} = \frac{\rho c}{A}$, where ρ, c, and A are the local mean density, speed of sound, and duct cross-sectional area, respectively [8,30]. For an ideal lossless discontinuity between two uniform plane-wave ducts, the pressure-amplitude reflection coefficient is $R_{\mathrm{p}} = \frac{Z_{\mathrm{c},2}-Z_{\mathrm{c},1}}{Z_{\mathrm{c},2}+Z_{\mathrm{c},1}}$. This relation provides a physical interpretation of the partial reflection caused by an impedance change; in the complete model, the effective reflection is additionally influenced by mean flow, losses and the dynamic loading of connected branches.

Distributed damping arises through wall friction and visco-thermal losses carried by $\boldsymbol{S}_{\mathrm{w}}$ and grows with frequency and propagation distance [31]. Together, these mechanisms, reflection at impedance discontinuities, phase accumulation along duct segments, and distributed dissipation, govern the standing-wave patterns and frequency-dependent transmission behavior of the exhaust network, and they provide the physical language used to interpret the sensitivity results in Section 3.

The plane-wave interpretation is valid only up to the first higher-order transverse duct mode, above which additional modal structure appears that Eq. (1) cannot resolve; the corresponding cut-on frequency for the present exhaust system is evaluated in Section 2.4. Equation (1) is advanced in the time domain over the entire flow network until cycle-to-cycle periodic convergence is reached, with the specific solver setup and convergence criterion detailed later in this section. The governing equations were solved in the time domain, with GT-POWER 2026 used as the numerical implementation platform [25].

The computational domain followed the measured intake and exhaust flow paths of the Wärtsilä 4L20 engine and included the compressor, charge-air cooler, intake manifold, four cylinders, twin-scroll turbine, and downstream exhaust network, as shown in Fig. 4. Pipes, bends, and junctions were represented as cross-sectionally averaged one-dimensional flow elements dimensioned from the measured geometry, while the valve boundary conditions used measured discharge coefficients. The baseline discretization lengths were $dX = 88$ mm on the intake side and $dX = 110$ mm on the exhaust side; their

Table 1
Specification of the research engine.

Configuration	Inline, 4-cylinder
Bore/stroke	200 mm / 280 mm
Compression ratio	15.8
Displacement	8.8 L per cylinder
Rated speed/ power	1000 rpm / 0.8 MW
Turbocharger	Accelleron TPS48E01; single-stage turbocharger; water-cooled charge-air cooler
Engine control	Rapid prototyping platform (Speedgoat)

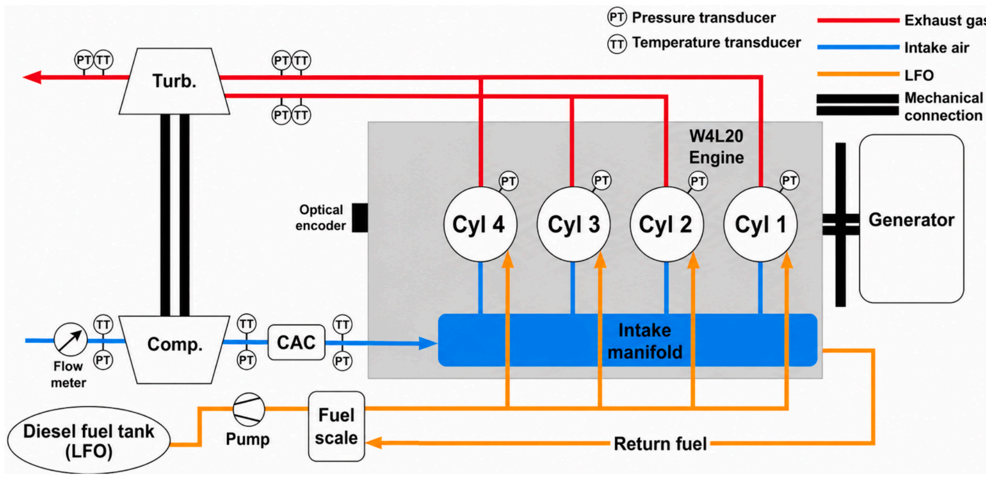

Fig. 1. Schematic of the Wärtsilä 4L20 research engine and its instrumentation, showing the intake and exhaust paths and the pressure and temperature transducer locations.

Table 2
Measurement systems used to characterize acoustic excitation and acquire the in-duct pressure signals.

Measured quantity	Instrument/ transducer	Sampling rate	Measurement range	Accuracy/ nominal sensitivity
In-cylinder pressure	Kistler 6613CG1 with Kistler 4624AK amplifier	100 kHz	0–250 bar	<0.5 % FSO
Intake-port pressure	Kistler 4007D	100 kHz	0–10 bar	<1.0 % FSO
Pressure fluctuations upstream and downstream of the turbine	Kistler 4049B	100 kHz	0–10 bar	±0.08 % FS, typical
In-duct pressure downstream of the turbine	GRAS 40SC probe microphone	100 kHz	2 Hz–8 kHz	3 mV/Pa

acoustic adequacy is evaluated systematically in Section 3.3. Fig. 4 distinguishes the explicit downstream network used for acoustic analysis from the simplified downstream representation used in the performance-oriented baseline model.

Gas–wall heat transfer, entering through S_w in Eq. (1), was resolved predictively from the local wall-layer properties, boundary conditions, and initial wall temperatures, with the convective heat-transfer coefficients evaluated using the Colburn correlation. A semi-predictive CAC model was implemented with outlet temperature correlated to engine load. Combustion was modeled semi-empirically using derived burn-rate curves obtained from Three-Pressure Analysis (TPA) of measured intake, in-cylinder, and exhaust pressures [15]. The turbocharger was represented by a conventional map-based approach using manufacturer-supplied compressor and turbine performance maps.

The simulation was run under steady-state operation, with a brake mean effective pressure (BMEP) controller regulating the fuel-injection rate to hold the target load. Equation (1) was advanced with an explicit Runge–Kutta scheme [32] applied simultaneously to all connected sub-circuits, with a maximum ratio of 1000 between the flow and ordinary-differential-equation (ODE) time steps. Convergence was controlled based on residual monitoring of shaft speed and fuel-injection rate, with steady-state achieved when both parameters satisfied a fractional tolerance of 0.001 for at least five consecutive cycles. Simulations were executed on a Dell Intel Core i7 vPro workbench PC, with up to 100 cycles considered to achieve convergence of flow and thermal properties across all system components. The main input parameters for the validated operating points are summarized in Table 3, and the corresponding one-dimensional model layout is shown in Fig. 4.

This calibrated steady-state model provides a reliable representation of the baseline engine performance and serves as the foundation for the acoustic and parametric analyses discussed in the following sections.

2.3. Modeling assumptions for acoustic simulations

With the validated baseline established, two distinct acoustic simulation purposes were considered. The measured–simulated in-duct spectral comparisons were performed at the acoustic measurement condition, corresponding to 1000 rpm and 400 kW. This operating point was therefore used for the acoustic validation figures and the associated error metrics. In contrast, the parametric sensitivity studies were conducted, unless stated otherwise, at the loudest simulated operating point, 100 % load at 1000 rpm (Table 3, row 100 %). This condition yields the highest exhaust mass flow and temperature, the strongest periodic excitation of the turbine and exhaust pipes, and the largest predicted outlet SPL; it was therefore selected to make the relative influence of modeling choices more distinguishable. Consequently, the 100 % load cases are interpreted as controlled parametric sensitivity studies rather than direct measurement-validation cases.

2.3.1. Exhaust stack modeling and noise sensor configuration

In the baseline performance model, as seen in Fig. 4, the exhaust system is simplified to two short pipes after the turbine outlet. For steady performance simulations, the downstream exhaust stack is accounted for through an equivalent flow restriction calibrated to reproduce the measured mean pressure drop. While this simplification is sufficient for predicting backpressure and overall engine performance, it does not capture the propagation, reflection, and interference of unsteady pressure waves in the downstream ducting, which govern the spectral characteristics of exhaust noise. To capture these effects, the exhaust pipeline was modeled explicitly, as highlighted in Fig. 4, using the actual geometry of the 4L20 research engine at the VEBIC laboratory. The implemented configuration includes the actual pipe lengths, diameters, bends, and junctions downstream of the turbine. This explicit representation preserves the physical wave propagation path and the principal geometric discontinuities responsible for acoustic reflection and interference within the one-dimensional (1D) framework. Silencers and after-treatment components were excluded from the sensitivity models to isolate the influence of the explicitly modeled duct network. Their omission does not imply that their upstream acoustic influence is

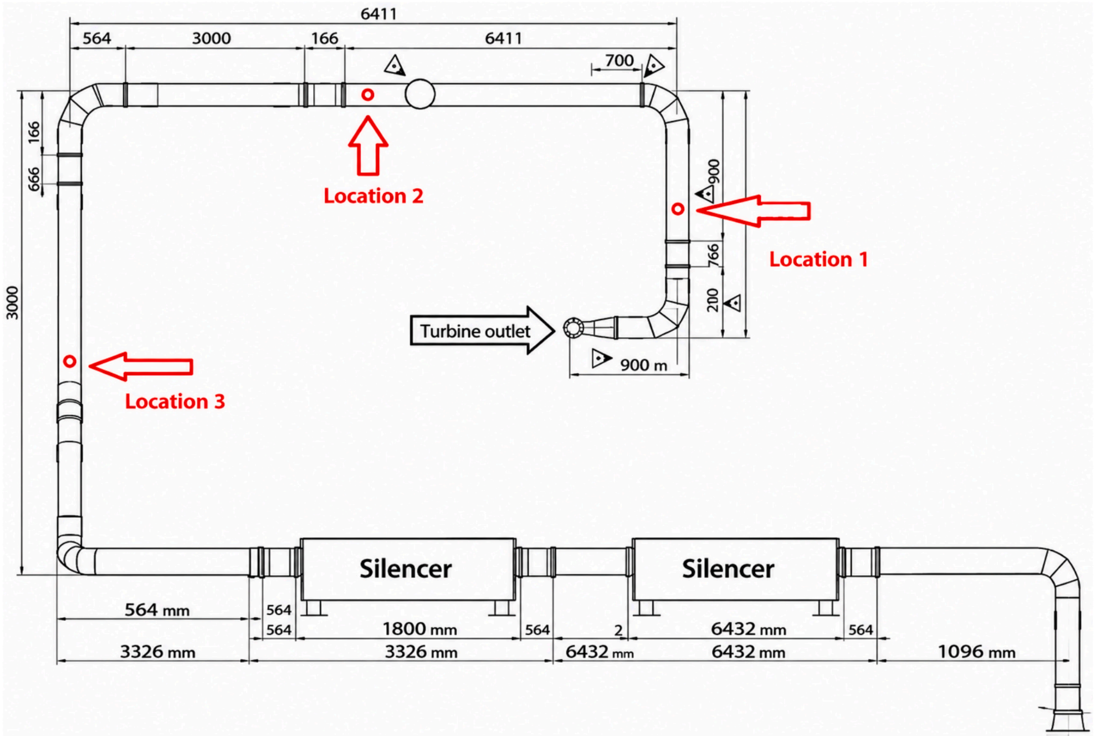

Fig. 2. Schematic of the exhaust stack downstream of the turbine, indicating in-duct measurement Locations 1–3.

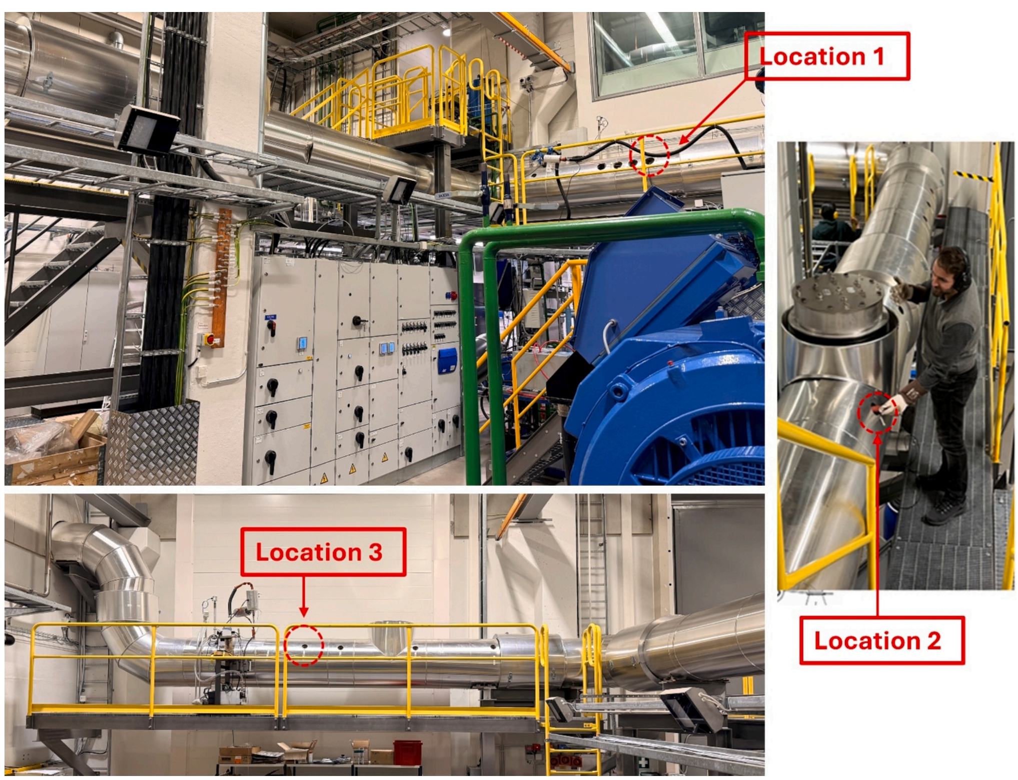

Fig. 3. In-duct pressure-measurement ports installed along the exhaust pipeline downstream of the turbine.

negligible: the frequency-dependent inlet impedance of a silencer can produce reflected waves in addition to transmission and attenuation [8]. The possible effect of these reflections on the in-duct validation is considered explicitly in Section 3.7.

The computational exhaust domain was terminated by prescribing the ambient static pressure and temperature at the outlet. This idealized open-boundary treatment defines the mean discharge condition but does not represent the complete frequency-dependent radiation impedance of the physical termination. Gas–wall heat transfer along the exhaust system was calculated from the local wall-layer properties, boundary

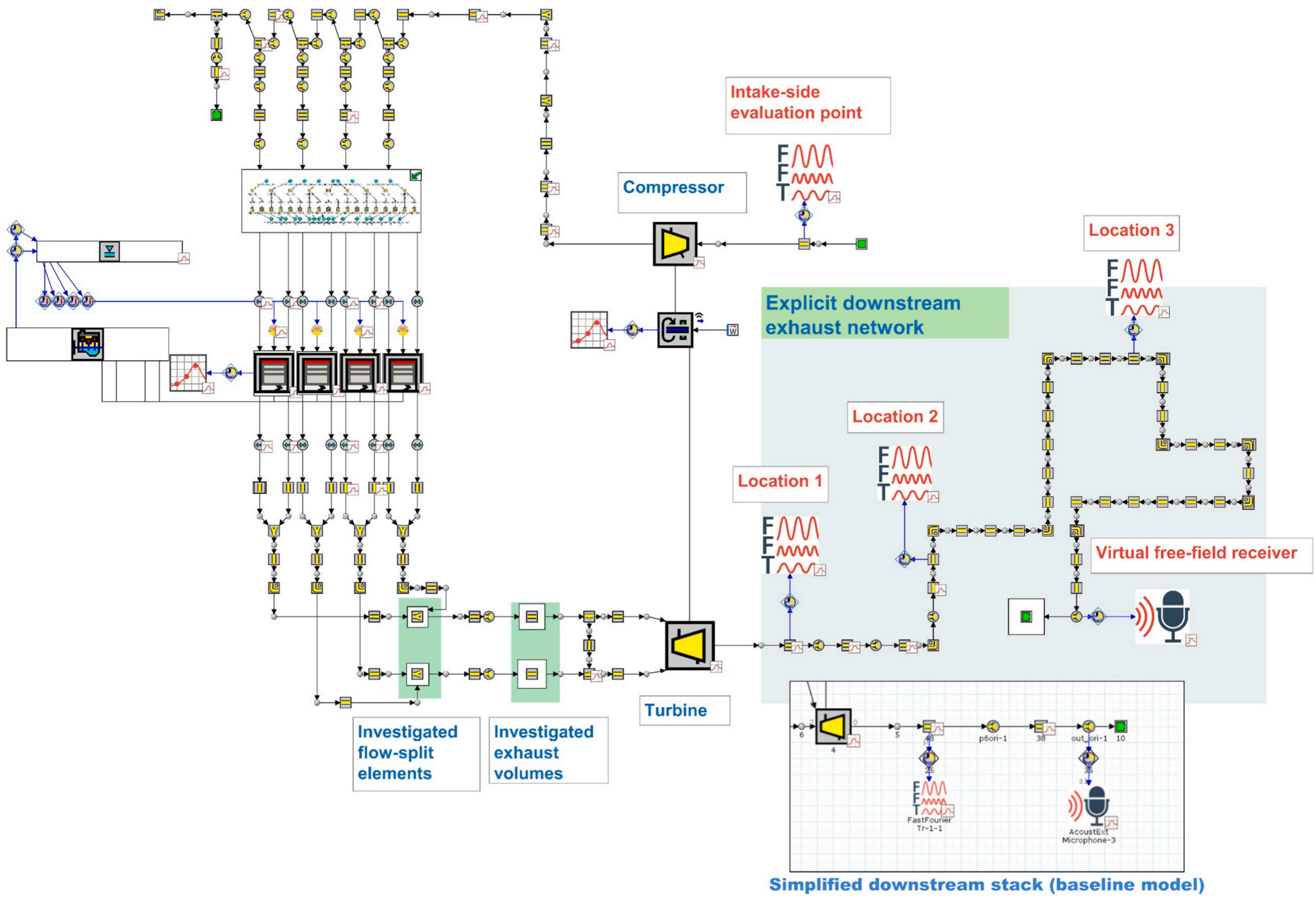

Fig. 4. One-dimensional engine model used in the acoustic study. The complete model is shown together with the explicitly represented downstream exhaust stack used in the acoustic simulations (highlighted area). The inset shows the simplified downstream exhaust-stack representation used in the performance-oriented baseline model. Also indicated are the studied flow-split and exhaust-volume elements, the in-duct spectral evaluation locations, the intake-side evaluation point, and the virtual free-field microphone position.

Table 3
Operating points and key input parameters used for steady-state model validation.

Load (%)	Engine speed (rpm)	BMEP (bar)	TC initial speed (rpm)
100	1000	25.0	47,500
85	1000	21.25	47,500
75	1000	18.75	47,500
50	1000	12.50	47,500
25	1000	6.25	20,000

conditions, and initial wall temperatures using the correlation-based formulation described in Section 2.2. The resulting gas-temperature distribution determines the local speed of sound and therefore influences the phase accumulation and propagation of pressure waves through the exhaust ducts [8]. The in-duct pressure was evaluated at the positions shown in Fig. 4. For the model-to-model sensitivity comparisons, the pressure at a receiver 1 m downstream of the exhaust outlet was reconstructed from the simulated outlet volumetric acceleration using the compact-monopole relation defined in Eq. (4). The assumptions and limitations of this radiation approximation are specified in Section 2.4. Accordingly, the resulting free-field spectra are interpreted only as relative sensitivity indicators, whereas all model-to-measurement validation is based on the in-duct pressure spectra.

2.3.2. Reduced-order acoustic representation of the turbocharger

The turbocharger affects engine noise through both active and passive acoustic mechanisms. Active noise arises mainly from the high-speed rotation of the turbine and compressor, generating broadband and blade-passing tonal components at higher frequencies [33]. This phenomenon is best captured using detailed 3D CFD, which is beyond the scope of typical 1D simulations. In contrast, the passive acoustic response—how the turbocharger geometry (volute, blades, and rotor) reflects, transmits, and absorbs pulsating-flow noise—is crucial for low- and mid-frequency exhaust-noise propagation. This response is not captured by performance-oriented simulations because turbocharger operation is represented using steady-state maps. In addition, the compressor and turbine maps are generated by a steady-state flow test rig that does not incorporate pulsating or unsteady behavior. To predict the acoustic performance of the entire exhaust or intake system on a turbocharged engine, a passive acoustic model of the turbocharger is required that incorporates representative internal geometry [26].

The compressor was represented by a discretized geometry-based acoustic model, defined through its inlet and outlet diameters, wheel size, volute area-to-radius ratio, and cross-sectional area distribution. The key geometric parameters of the Accelleron Industries AG (Switzerland) TPS48E01 compressor were provided directly by the manufacturer. This configuration enables the model to capture the compressor's passive transmission and reflection behavior, allowing the intake-side acoustic effects to be assessed in the overall exhaust noise analysis [25]. Because the discretized compressor introduces additional geometric detail and flow resistance, its integration was constrained to reproduce the baseline (map-based) operating point: a compressor mass-flow multiplier of 1.04 was combined with calibrated flow discharge coefficients, so that the compressor mass flow, pressure ratio, and the resulting engine operating point matched the map-based reference.

The acoustic turbine model followed the reduced-order geometry-based approaches of Elnemr [33] and Serrano et al. [26]. The turbine was represented by coupled zero-dimensional (0D) and one-dimensional (1D) gas-dynamic elements connected to a conventional turbine performance-map element, as illustrated in Fig. 5. The performance-map element retained the steady-flow expansion, efficiency, and shaft-work characteristics, whereas the additional elements introduced finite wave-propagation paths, acoustic storage, impedance discontinuities, and associated expansion and visco-thermal losses. Under the linearized plane-wave approximation, the storage, phase, and characteristic-impedance scales are defined by Eq. (3) [8,30]:

$$Z_{c,i} = \frac{\rho_i c_i}{A_i}, \qquad \phi_i^{\pm} = k_i^{\pm} L_i, \qquad k_i^{\pm} = \frac{\omega}{c_i \pm U_i}, \qquad C_{a,i} = \frac{V_i}{\rho_i c_i^2} \tag{3}$$

where $Z_{c,i}$ is the local characteristic impedance, $\phi_i^{\pm}$ is the phase accumulated across an element of length L_i, and $C_{a,i}$ is the acoustic compliance associated with a compact gas volume V_i. The equivalent elements of the turbine model were therefore dimensioned to reproduce these three quantities rather than the physical geometry, and the resulting parameters are listed below.

The tongue and volute were represented as straight, circular, constant-area equivalent ducts with acoustic volumes of 0.563 and 0.992 L and length-to-diameter ratios of approximately 0.6 and 1.5, respectively. These values correspond to equivalent diameter–length pairs of approximately 106 mm × 64 mm for the tongue and 94 mm × 142 mm for the volute. The rotor was represented as an acoustically compact volume of 1.70 L. The outlet was represented by the expanding equivalent duct shown in Fig. 5, with a volume of 2.48 L and an outlet-to-inlet area ratio of approximately 1.5. The reported quantities disclose the acoustic storage, phase-length scales, and principal impedance ratios of the reduced-order model; they are not intended to reconstruct the proprietary blade-passage geometry. The operating-point transmission loss reported in Section 3.6 therefore provides a model-internal numerical characterization of the adopted representation at the full-load sensitivity condition.

Heat transfer and correlation-based friction losses were disabled, while realistic expansion and visco-thermal losses were retained to reproduce the expected pressure drops. Because the added geometric detail introduces only minor deviations from the baseline, the turbine's steady-state operating point was preserved without turbine-side re-tuning, and no mass multipliers were applied to the turbine. The downstream-orifice diameter, which belongs to the performance-calibration stage and sets the simplified exhaust back-pressure, was not altered for the acoustic substitution. The consistency of the mean operating point before and after the substitution is quantified in Section 3.6.

The passive acoustic behavior of the reduced-order turbine representation was characterized by its transmission loss (TL), evaluated on a dedicated numerical two-port bench (Fig. 6) using two-port, four-microphone plane-wave decomposition. A broadband white-noise source was placed upstream and an anechoic termination downstream,

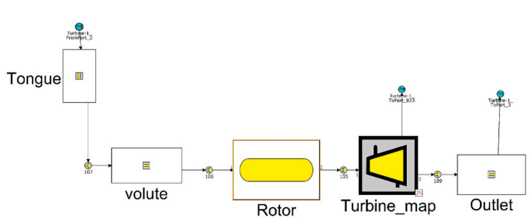

Fig. 5. Topology of the reduced-order acoustic turbine model, comprising equivalent straight tongue and volute ducts, a lumped rotor volume, the turbine performance-map element, and an equivalent tapered outlet duct.

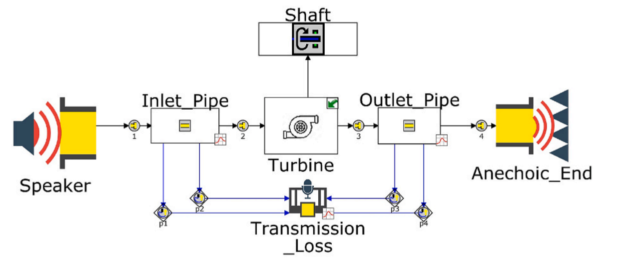

Fig. 6. Numerical acoustic two-port bench used to evaluate the turbine transmission loss: broadband white-noise source, four-microphone plane-wave decomposition, and anechoic termination.

with two 50 mm microphone pairs positioned upstream and downstream to decompose the pressure field into forward- and backward-travelling components. The bench was run at the turbine operating point (1000 rpm and 100 % load; inlet mean velocity 117 m/s; inlet temperature 806 K; velocity-perturbation amplitude 0.5 m/s), with mean-flow convection (Mach ≈ 0.2) retained in the wave separation. Because the bench employs the same reduced-order turbine representation as the engine model, the resulting TL provides an internal numerical check of its two-port behavior at this operating point. As no measured turbine transfer matrix or experimental TL dataset was available, the results are used to characterize the model response and are not interpreted as independent experimental validation of the physical turbocharger.

2.3.3. *Scope of simulations*

To evaluate how modeling fidelity and exhaust-side geometry influence the predicted exhaust-noise response, four targeted simulation campaigns were performed using the acoustic model described in Section 2.3.1 and shown in Fig. 4. In each campaign, only the parameters under investigation were varied, while the operating point, combustion model, boundary conditions, and all other model settings were kept unchanged. For campaigns C1–C4, the fixed operating point was the 100 % load, 1000 rpm parametric condition, whereas the measured 1000 rpm and 400 kW condition was retained for the direct in-duct acoustic validation. This approach provides controlled comparisons between model configurations. Since pipe and junction variations may also modify local mass flow, pressure, temperature, velocity, and flow losses, Campaigns C2 and C3 are interpreted as coupled thermo-fluid–acoustic sensitivities rather than as isolated acoustic effects. The scope of the simulations is summarized in Table 4.

Campaign 1 examined the influence of spatial discretization length, *dX*, on the predicted acoustic response. The baseline performance-oriented mesh corresponded to 110 mm in the exhaust system and 88 mm in the intake system, while the acoustic reference discretization was defined as half of these values. From this starting point, exhaust-side and intake-side meshes were refined separately, down to 30 % of the acoustic *dX* on the exhaust side and 50 % on the intake side, to assess the numerical resolution required for reliable SPL prediction. The comparison included free-field and in-duct SPL spectra, agreement relative to the finest mesh, and computational runtime. Because the explicit time step was constrained by the local Courant–Friedrichs–Lewy condition [24], each reduction in the prescribed spatial discretization length also produced a corresponding reduction in the time step. Campaign C1 therefore represents a coupled spatial–temporal discretization sweep rather than an independent variation of spatial resolution alone.

In campaign 2, the influence of exhaust-path geometric volume was examined by varying the length and diameter of selected upstream exhaust pipe sections in Fig. 4 by ± 20 % relative to the reference geometry. This variation range is sufficient to reveal systematic shifts in acoustic interference and resonance behavior while remaining within realistic engineering tolerances during early design iterations.

In campaign 3, the sensitivity of junction modeling was evaluated by

Table 4
Summary of the four simulation campaigns and parameter variations.

Campaign	Component/location	Parameter(s) swept	Reference case	Variation range	Notes/outputs tracked
C1: Spatial resolution	Whole model (intake and exhaust ducts)	Discretization length dX	Exhaust: 110 mm; Intake: 88 mm	Refinement up to 30 % of acoustic dX	SPL spectra (free-field and in-duct), runtime, correlation/RMSE vs. refined reference
C2: Exhaust volume definition	Selected upstream exhaust pipe section	Pipe length and diameter	L = 300 mm, D = 73 mm	±20 % relative to reference geometry	Free-field SPL trends; shift of spectral peaks/dips due to resonance effects
C3: Junction modeling	Flow split elements upstream of turbine (Exh_FS)	Characteristic length, expansion diameter	L = 90 or 150 mm; D = 76 mm	±20 % relative to reference values	Sensitivity of SPL to junction representation and wave scattering
C4: Turbocharger acoustic representation	Compressor and turbine	Whole sub-model change	Performance-map representation	Geometry-based compressor and turbine models	Free-field SPL and turbine transmission loss

varying the characteristic length and expansion diameter of selected flow split elements upstream of the turbine (Fig. 4) by ± 20 % relative to the reference configuration. These parameters define the effective propagation distance and cross-sectional transition within the junction element and therefore influence acoustic reflection and transmission behavior in the exhaust network.

Across all four campaigns, the predicted response was evaluated primarily from narrowband SPL spectra at the exhaust outlet and, where relevant, at selected in-duct locations. Computational runtime was additionally monitored for the discretization campaign. For Campaigns C2 and C3, no separation is made between impedance- and phase-related acoustic effects and accompanying changes in the local mean-flow and loss characteristics.

2.4. Post-processing of simulation results

The signal-processing parameters used for the spectral analyses are summarized in Table 5. Post-processing of simulation and experimental data was carried out using a common procedure so that all quantities shown in Section 3 are directly comparable. For the model-to-model free-field sensitivity analysis, the outlet volume velocity $Q(t) = Su_o(t)$ was treated as a compact monopole. Assuming spherical propagation, the acoustic pressure at a receiver located at a distance r from the outlet was calculated following Eq. (4).

$$p_f(t) = \frac{\rho_\infty S}{4\pi r}\frac{\mathrm{d}}{\mathrm{d}t}\left[u_o\left(t - \frac{r}{c_\infty}\right)\right] \tag{4}$$

Table 5
Signal-processing parameters used for the spectral analyses.

Parameter	In-duct validation	Free-field sensitivity analysis
Analysis record	Final 0.12 s engine cycle; 12,000 samples at 100 kHz	Same
Window	Hann; one engine cycle	Same
Overlap and averaging	One complete cycle; no ensemble averaging	Same
Record construction	Direct 0.12 s cycle; no repetition, extension, interpolation, or resampling	Direct 0.12 s cycle
FFT-bin spacing	8.33 Hz	8.33 Hz
Quantitative validation range	8.33–633.33 Hz (76 Fourier lines)	—
Spectral settings	0–1000 Hz; single-sided RMS; $p_0 = 2 \times 10^{-5}$ Pa	Same
Radiation formulation	—	Compact spherical monopole; receiver 1 m downstream
Ambient properties	—	$\rho_\infty = 1.17$ kg/m^3; $c_\infty = 346$ m/s
Excluded effects	—	Radiation impedance/end correction, exterior mean-flow convection, flow noise, ground effects and empirical transfer-function shaping

Here, the parameters ρ_∞ and c_∞ denote the ambient density and speed of sound, respectively; S is the outlet area, u_o is the outlet velocity, and $r =$ 1 m is the receiver distance [30]. Equation (4) represents compact spherical radiation from the outlet volume-flow fluctuation; it is not a complete acoustic model of the physical exhaust termination.

The outlet boundary was defined by the ambient static pressure and temperature. The formulation did not include a frequency-dependent radiation impedance, open-end correction, mean-flow convection in the exterior field, jet-mixing noise, the thermal transition between the hot exhaust and ambient gas, ground reflection, or an empirical radiation transfer function. The compact-monopole approximation is most appropriate when $ka \ll 1$ and the outlet Mach number is low, where k is the acoustic wavenumber and a is the outlet radius. For a duct exhausting hot gas, the radiation impedance and reflected-wave behavior can depend on Helmholtz number, mean-flow Mach number, and the exhaust-to-ambient temperature ratio [34].

The same outlet geometry, receiver location and monopole formulation were applied to every simulated configuration, providing a consistent basis for model-to-model comparison. This common treatment does not imply exact cancellation of the neglected radiation effects because the investigated refinements may alter the amplitude and phase of the outlet-velocity fluctuation, as well as the local temperature and mean-flow state. Accordingly, the free-field spectra are interpreted only as relative sensitivity indicators within the adopted radiation approximation, not as validated absolute predictions of radiated sound. No free-field result is compared with measurement, and all quantitative model validation is based on the in-duct spectra. Uncertainty in the simplified outlet termination may nevertheless affect the upstream pressure field through reflected waves and is retained as a model limitation.

The in-duct validation used the final complete 720° CA window from each record: the final simulated cycle and measured cycle 87. Cycle 87 was selected because it is the last complete measured cycle before the trailing partial record, not on the basis of agreement with the model. At 1000 rpm, each window lasts 0.12 s and contains 12,000 samples at 100 kHz, giving the native Fourier-line spacing $\Delta f = 1/T = 8.33$ Hz. After removal of the cycle mean, measured and simulated signals were processed identically using a symmetric Hann window and single-sided RMS normalization. No ensemble average was used for the displayed validation spectrum; all 87 complete measured cycles were used separately to quantify repeatability and the robustness of the MAE comparison.

All quantitative in-duct validation results were calculated directly on this native 8.33 Hz grid. The measured cycle was not periodically repeated, the record was not extended, and no zero padding, time-domain interpolation, frequency-domain interpolation, resampling, or model retuning was applied. The below-cut-on comparison therefore uses the 76 positive-frequency Fourier lines from 8.33 to 633.33 Hz. Spectral content from 641.67 to 1000 Hz is retained only for descriptive continuity in the figures and is excluded from the quantitative validation metrics. The free-field sensitivity spectra were likewise evaluated directly at the native 8.33 Hz spacing.

At each spectral line, SPL was calculated from the single-sided RMS amplitude $p_{\mathrm{rms}}(fk)$ as

$$L_{\mathrm{p}}(f_k) = 20\log_{10}\left[\frac{p_{\mathrm{rms}}(f_k)}{p_0}\right], \qquad p_0 = 2\times10^{-5}\,\mathrm{Pa} \tag{5}$$

In Eq. (5), p_0 is the internationally standardized reference sound pressure for airborne sound [35].

The upper limit of the quantitative validation was determined from the plane-wave assumption underlying the one-dimensional acoustic formulation. Above the first higher-order-mode cut-on frequency, transverse modes can propagate, and the in-duct acoustic field can no longer be represented solely by the plane-wave mode [36]. Using the rigid-walled circular-duct approximation adopted in the present study, the first higher-order-mode cut-on frequency was estimated from Eq. (6),

$$f_{\mathrm{c},10} = \frac{j'_{1,1}c}{\pi D} = \frac{1.841c}{\pi D} \tag{6}$$

where $j'_{1,1} = 1.841$ is the first non-zero root of the derivative of the first-order Bessel function, c is the local speed of sound, and D is the duct diameter. For the largest duct section and its corresponding local gas temperature, Eq. (6) gives a cut-on frequency of approximately 640 Hz. This value is adopted as a conservative network-wide screening limit for quantitative validation rather than as a uniform local cut-on frequency throughout the exhaust system. The local cut-on frequency varies with both duct diameter and gas temperature and is generally higher in the smaller-diameter sections. Spectral content above 640 Hz is retained in the figures but is interpreted only as an equivalent plane-wave trend because higher-order duct modes may contribute. The below-cut-on validation diagnostics reported in Section 3.7 are therefore evaluated on the available native Fourier lines from 8.33 to 633.33 Hz.

Engine-order amplitudes were evaluated to quantify agreement at the deterministic firing components. Engine order was defined relative to the crankshaft rotational frequency as $n = f/f_{\mathrm{rot}}$, where $f_{\mathrm{rot}} = N/60$. At 1000 rpm, $f_{\mathrm{rot}} = 16.67$ Hz. For a four-cylinder four-stroke engine with evenly spaced firing, two firing events occur per crankshaft revolution; consequently, the fundamental firing component occurs at order $n = 2$, with harmonics at the subsequent even orders. The firing-order mean absolute error (MAE) was evaluated at $n = 2, 4, \ldots, 12$, corresponding to 33.3–200 Hz. These six frequencies coincide with native 8.33 Hz Fourier lines. The metric is the arithmetic mean of the absolute measured–simulated SPL differences at the selected orders.

One-third-octave-band levels were calculated directly from the native in-duct Fourier-line mean-square pressures. Energetic summation was performed within the exact base-10 band limits specified in IEC 61260–1 [37] for nominal center frequencies from 16 to 500 Hz. At the native 8.33 Hz spacing, the nominal 20 Hz band contains no Fourier line and was omitted; the reported one-third-octave RMSE therefore uses the other 15 non-empty bands. Band levels were obtained by summing single-sided RMS line powers rather than arithmetically averaging decibel values. This aggregation changes the representation of the supported line powers but does not create additional spectral information.

Mean spectral SPL was defined as the arithmetic mean of the native narrowband SPL ordinates on the fixed 8.33 Hz grid, with the DC ordinate excluded. It is a descriptive average of the logarithmic line levels and is not an energy-integrated overall sound pressure level. It was evaluated over the plane-wave-valid range from 8.33 to 633.33 Hz, that is, the same 76 Fourier lines used for the other validation metrics. The measurement uncertainty was evaluated separately for this same mean-SPL statistic. The standard uncertainty of the calibrated GRAS 40SC measurement chain was estimated as $u_{\mathrm{inst}} \approx 0.40$–$0.45$ dB, combining the available calibrator-accuracy, microphone-sensitivity and drift, and acquisition-chain contributions. Following the Guide to the Expression of Uncertainty in Measurement (GUM) [38], independent contributions were combined as:

$$u_{\mathrm{c}} = \sqrt{u_{\mathrm{inst}}^2 + u_{\mathrm{rep,mean}}^2} \quad , U_{95} = 2u_{\mathrm{c}} \tag{7}$$

In Eq. (7), $u_{\mathrm{rep,mean}}$ is the Type-A repeatability contribution. Using the same mean removal, symmetric Hann taper, native 8.33 Hz grid, and arithmetic mean-SPL definition for all 87 complete measured cycles, the cycle-to-cycle standard deviations of this statistic were 0.356 dB at Location 1 and 0.443 dB at Location 3. For a conservative common uncertainty, the larger repeatability contribution and the upper instrument estimate were adopted. This gives an expanded uncertainty $U_{95} = ku_{\mathrm{c}}$ of $\pm$ 1.3 dB for $k = 2$. A single bound is quoted because the same statistic is reported at both stations; evaluated separately with the same 0.45 dB instrument term, the corresponding values are $\pm$ 1.15 dB at Location 1 and $\pm$ 1.26 dB at Location 3. The $\pm$ 1.3 dB value therefore provides a rounded common upper bound. It applies only to the arithmetic mean-SPL results and is distinct from the metric-specific MAE uncertainties reported below.

Measurement-related uncertainty in the narrowband MAE was evaluated by recalculating the metric for each model against each of the 87 complete measured cycles over the same 76 Fourier lines. The resulting cycle-to-cycle standard deviations were 0.331, 0.281 and 0.338 dB for simplified Location 1, refined Location 1 and refined Location 3, respectively. For a uniform calibration offset, the MAE sensitivity coefficient is the magnitude of the mean sign of the line-by-line errors. The coefficients calculated from the selected spectra are 0.158, 0.263 and 0.368 (0.16, 0.26 and 0.37 to two decimal places), respectively; their values below unity reflect the mixed signs of the line errors. A conservative unit coefficient was nevertheless retained. With the upper instrument standard uncertainty of 0.45 dB, Eq. (7) then gives $U_{95} = \pm 1.12$, ± 1.06 and $\pm$ 1.13 dB for $k = 2$. Using the calculated coefficients would instead give $\pm$ 0.68, ± 0.61 and $\pm$ 0.75 dB. The reported intervals therefore deliberately bound measurement-related variability in MAE; they exclude model-form and input uncertainties and are not model-acceptance limits.

Agreement between simulated and measured spectra was quantified using three complementary metrics: the narrowband MAE (average magnitude of the line-by-line error), the Pearson correlation coefficient, r (spectral-shape similarity, independent of absolute level), and the RMSE (overall level deviation over the evaluated band). The narrowband MAE is the arithmetic mean of the absolute simulated–measured SPL differences over the 76 below-cut-on Fourier lines; unlike RMSE, it weights the absolute errors linearly. The Pearson correlation coefficient and RMSE are defined over the N frequency bins of the evaluated band in Eq. (8) and Eq. (9), respectively, where $\mathrm{SPL}_{\mathrm{sim}}$ and $\mathrm{SPL}_{\mathrm{meas}}$ denote the simulated and measured narrowband sound-pressure levels, respectively, and the overbar denotes the band-averaged value.

$$\mathrm{RMSE} = \sqrt{\frac{1}{N}\sum_{i=1}^{N}\left[\mathrm{SPL}_{\mathrm{sim}}(f_i) - \mathrm{SPL}_{\mathrm{meas}}(f_i)\right]^2} \tag{8}$$

$$r = \frac{\sum_{i=1}^{N}\left(\mathrm{SPL}_{\mathrm{sim},i} - \overline{\mathrm{SPL}}_{\mathrm{sim}}\right)\left(\mathrm{SPL}_{\mathrm{meas},i} - \overline{\mathrm{SPL}}_{\mathrm{meas}}\right)}{\sqrt{\sum_{i=1}^{N}\left(\mathrm{SPL}_{\mathrm{sim},i} - \overline{\mathrm{SPL}}_{\mathrm{sim}}\right)^2 \sum_{i=1}^{N}\left(\mathrm{SPL}_{\mathrm{meas},i} - \overline{\mathrm{SPL}}_{\mathrm{meas}}\right)^2}} \tag{9}$$

The bias-removed RMSE reported in Section 3.7 isolates the dispersion of the line-by-line errors from any uniform level offset. With $e_{\mathrm{i}} = \mathrm{SPL}_{\mathrm{sim}}(f_{\mathrm{i}}) - \mathrm{SPL}_{\mathrm{meas}}(f_{\mathrm{i}})$ denoting the error at each Fourier line and $\bar{e}$ its arithmetic mean, it is defined by Eq. (10):

$$\mathrm{RMSE}_{\mathrm{BR}} = \sqrt{\frac{1}{N}\sum_{i=1}^{N}\left[e_i - \bar{e}\right]^2} \tag{10}$$

The two quantities are related by the exact decomposition $\mathrm{RMSE}^2 = \mathrm{RMSE}_{\mathrm{BR}}^2 + \bar{e}^2$, so the total RMSE combines the signed mean error and the dispersion of the line-by-line errors. A reduction in bias-removed RMSE therefore indicates a smaller scatter of the frequency-by-frequency errors rather than a change in overall level, and the two terms can move in opposite directions.

The turbine transmission loss (TL) was evaluated from the two-port bench described in Section 2.3.2 (Fig. 6). With mean flow present in each duct, plane-wave perturbations propagate with convected wavenumbers $k^{\pm} = \omega/(c \pm U) = k/(1 \pm M)$, where $M = U/c$ is the local Mach number [8]. From the complex pressures P_1 and P_2 measured at two microphones separated by a distance s, the forward and backward travelling-wave amplitudes are recovered by two-microphone plane-wave decomposition, Eq. (11) [8]:

$$P^{+} = \frac{P_1\,\mathrm{e}^{\mathrm{j}k^{-}s} - P_2}{\mathrm{e}^{\mathrm{j}k^{-}s} - \mathrm{e}^{-\mathrm{j}k^{+}s}}, \qquad P^{-} = \frac{P_2 - P_1\,\mathrm{e}^{-\mathrm{j}k^{+}s}}{\mathrm{e}^{\mathrm{j}k^{-}s} - \mathrm{e}^{-\mathrm{j}k^{+}s}} \tag{11}$$

The 50 mm microphone spacing on each pair keeps ks below approximately 0.6 rad across 0–1000 Hz at the bench exhaust-gas sound speed, which is well within the two-microphone decomposition range [8]. The acoustic power carried in each direction through a duct of cross-section A, corrected for mean-flow convection, is given by Eq. (12):

$$W^{\pm} = \frac{|P^{\pm}|^2 A}{2\rho c}\,(1 \pm M)^2 \tag{12}$$

with local density ρ and sound speed c [8]. With the anechoic termination suppressing the downstream reflected wave, the downstream field is purely transmitted ($W^{-}_{\mathrm{ds}} \approx 0$), and TL follows from the ratio of incident to transmitted powers,

$$\mathrm{TL} = 10\log_{10}\left(\frac{W^{+}_{\mathrm{us}}}{W^{+}_{\mathrm{ds}}}\right) \tag{13}$$

In Eq. (13), subscripts us and ds denote the upstream and downstream ducts of the bench. No additional area correction was required because the local duct area is already included in the acoustic-power expression in Eq. (12). The four pressure signals were divided into successive analysis blocks, each tapered using a Hann window. The resulting single-sided auto-spectra were ensemble-averaged across the blocks to reduce estimation variance under broadband white-noise excitation. The reported quantity is therefore the downstream-direction incident-to-transmitted acoustic-power TL at the specified mean operating point, rather than a raw upstream–downstream SPL difference or an operating-point-independent characterization of the turbine [27,28].

In parallel, key engine performance parameters were extracted from the simulation output to cross-assess the impact of acoustic parameter variations. These included, among other measures, brake thermal efficiency (BTE) and brake mean effective pressure (BMEP) as a measure of produced torque independent of engine displacement. The methodology of calculation is standard in the engine domain. For details, the reader is referred to Heywood [39].

3. Results and discussion

Throughout Section 3, the signed spectral difference is defined as $\Delta\mathrm{SPL}(f) = \mathrm{SPL}_{\mathrm{case}}(f) - \mathrm{SPL}_{\mathrm{ref}}(f)$, where “case” is the configuration or spectrum named first and “ref” is the comparison spectrum named second. Negative values mean that the first-named case is lower than the reference; positive values mean that it is higher.

3.1. Baseline performance-model validation

The baseline 1D engine model is validated against measured data at 1000 rpm over four load points (25–100 %), using the calibration reported by Hautala et al. [40]. The total intake air mass flow is predicted to be within 3.7 %, and the intake manifold temperature matches within 1 K. BTE and BMEP show good agreement, with errors of less than 0.5 % and 0.6 %, respectively. This level of agreement indicates that the model reliably captures the gas exchange, combustion behavior, and heat transfer effects that significantly influence exhaust noise generation.

Fig. 7 compares the measured and baseline performance-calibrated narrowband SPL spectra at in-duct Location 1 for 1000 rpm and 400 kW using the direct 8.33 Hz Fourier-line spacing defined in Section 2.4. The upper panel presents the spectra, and the lower panel shows the signed spectral difference over 0–1000 Hz. Over the 76 below-cut-on lines from 8.33 to 633.33 Hz, the baseline comparison gives a narrowband RMSE of 11.42 dB and a Pearson correlation coefficient of $r = 0.736$. The deviations are strongly frequency-dependent and cannot be represented by a constant offset or simple scaling. Spectral content above the approximately 640 Hz cut-on frequency is shown descriptively only. These results indicate that performance calibration alone does not provide sufficient accuracy for predicting the post-turbine in-duct acoustic spectrum, which also depends on unsteady wave propagation, reflection, phase interaction, and numerical resolution.

The baseline deviation shown in Fig. 7 serves as the starting point for the remainder of the results discussion. In the following subsections, candidate parameters are varied individually to determine which factors most strongly influence the predicted spectrum and to explain why a performance-calibrated baseline is insufficient for exhaust-noise prediction.

3.2. Effect of downstream exhaust-stack representation on the predicted acoustic response

Fig. 8 compares the predicted free-field SPL spectra for the simplified and explicit-stack configurations. The updated comparison shows that the downstream stack does not act as a simple broadband attenuator. Although the explicit-stack configuration gives only a modest mean reduction, with mean $\Delta\mathrm{SPL} = 1.60$ dB, the spectral deviation is considerably larger than this average value suggests, with RMSE = 10.43 dB, mean absolute error (MAE) = 8.24 dB, and $r = 0.855$. Therefore, the two spectra retain a comparable global trend because the same engine excitation is used, but the explicit downstream exhaust stack geometry significantly redistributes the acoustic energy across frequency.

By extending the downstream ducting, the exhaust system’s effective acoustic length and boundary impedance are modified, which changes the phase accumulated by propagating waves and therefore shifts the frequencies at which reflected waves return in-phase or out-of-phase with the incident wave. In practice, this moves the interference pattern (peaks and notches) along the frequency axis. This behavior is consistent with classical duct standing-wave scaling, where the characteristic frequencies of resonance/anti-resonance features vary approximately inversely with the effective length of the acoustic path [30]. This modification not only shifts feature locations; it also changes their strength. Adding duct segments and discontinuities (bends, junctions, area changes, side volumes) modifies the local reflection coefficient magnitude at each impedance mismatch and increases the number of interacting reflection sites. As a result, peaks can become weaker or stronger, and notches can deepen or become shallower depending on how the multiple reflected components combine at the outlet. In addition, the increased propagation distance introduces frequency-dependent damping, which contributes to a gradual reduction of higher-frequency amplitudes [8]. However, the observed changes in peak and notch magnitudes are primarily governed by interference effects associated with modified reflection patterns.

Fig. 9 shows the predicted narrowband in-duct SPL spectra at the model extraction point corresponding to Location 1 immediately downstream of the turbine (Fig. 4) for the simplified and extended exhaust-stack configurations. In contrast to the more pronounced differences observed in the free-field response, the two in-duct spectra remain very closely aligned over the analyzed band, with a Pearson correlation coefficient of $r = 0.99$ and an RMSE of 1.76 dB. The mean

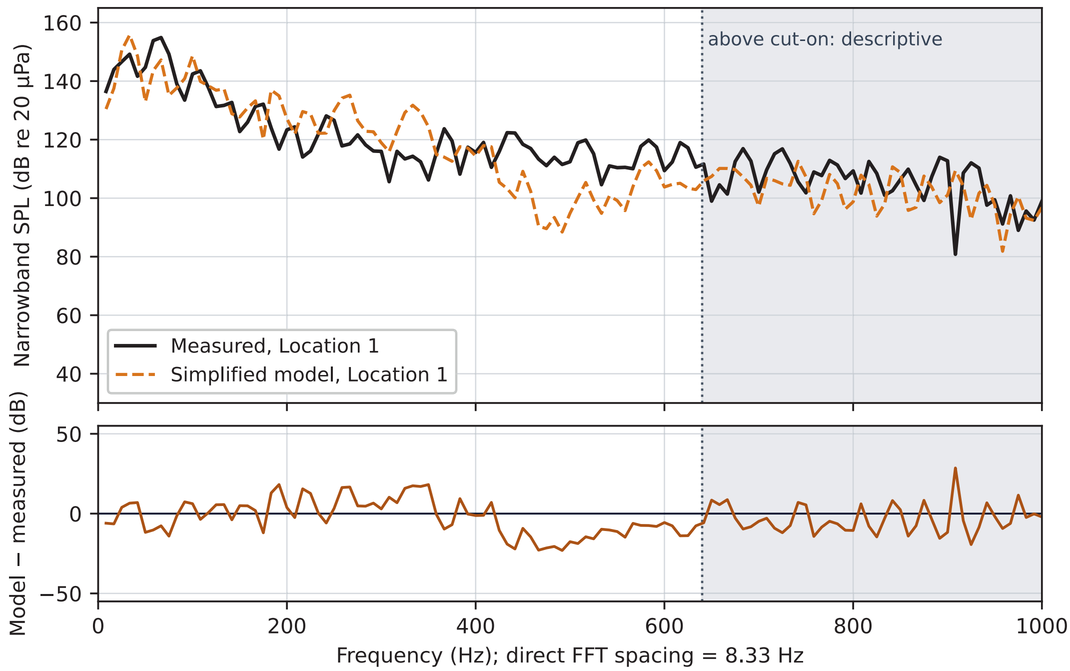

Fig. 7. Measured and baseline (performance-calibrated, 'simplified') narrowband in-duct sound pressure level at Location 1 (measurement position in Fig. 2; corresponding model extraction point in Fig. 4) at 1000 rpm and 400 kW, calculated directly from one complete 0.12 s cycle at the native 8.33 Hz Fourier-line spacing. Top: measured and simulated spectra; bottom: signed spectral difference. The vertical line marks the conservative cut-on screening limit of approximately 640 Hz; higher-frequency content is descriptive and is excluded from quantitative validation.

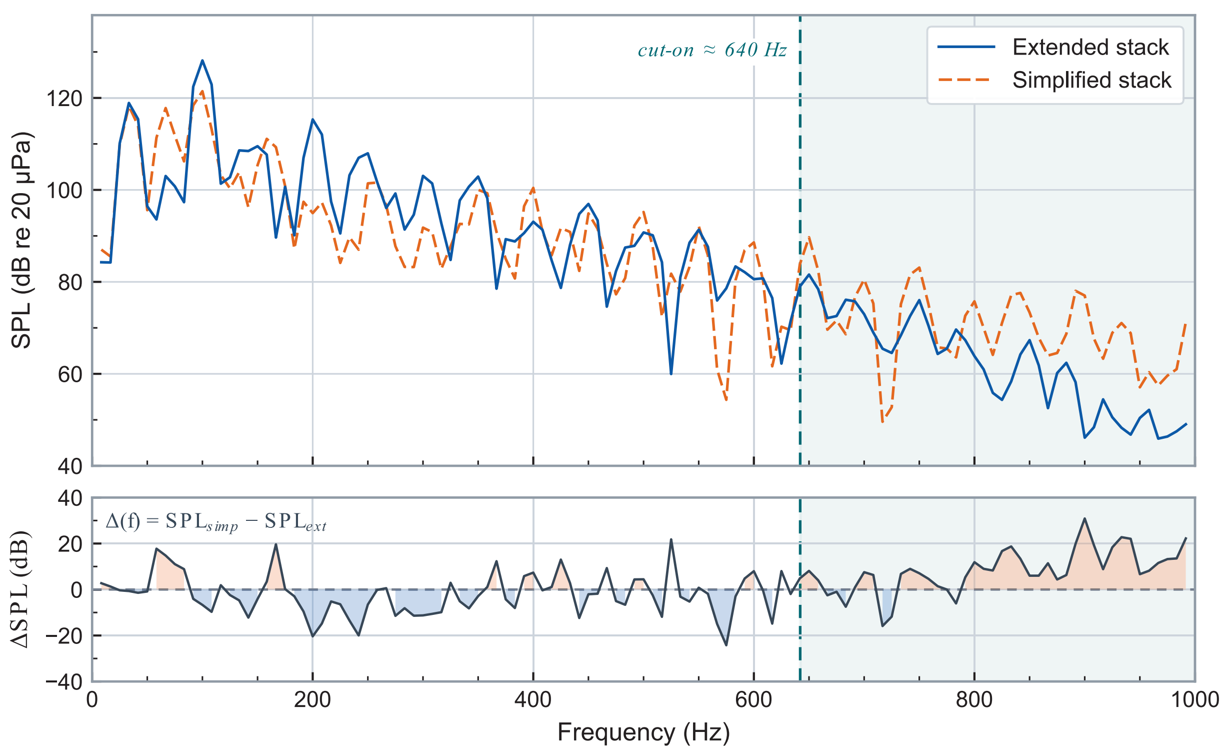

Fig. 8. Free-field SPL for the simplified and extended exhaust-stack configurations (virtual microphone 1 m downstream of the outlet; 1000 rpm, 100 % load). Top: spectra; bottom: signed difference.

signed difference is -0.18 dB, indicating that inclusion of the downstream stack does not introduce a meaningful systematic level shift at this upstream in-duct location. The remaining differences are mainly frequency-local, appearing as small changes in the depth and position of individual peaks and notches rather than as a broadband attenuation trend. This behavior is consistent with classical duct-acoustic theory. The downstream extension modifies the propagation path, impedance distribution, and outlet condition of the exhaust system, but only a reduced portion of the downstream-generated reflected wave field propagates back to the post-turbine location after partial transmission,

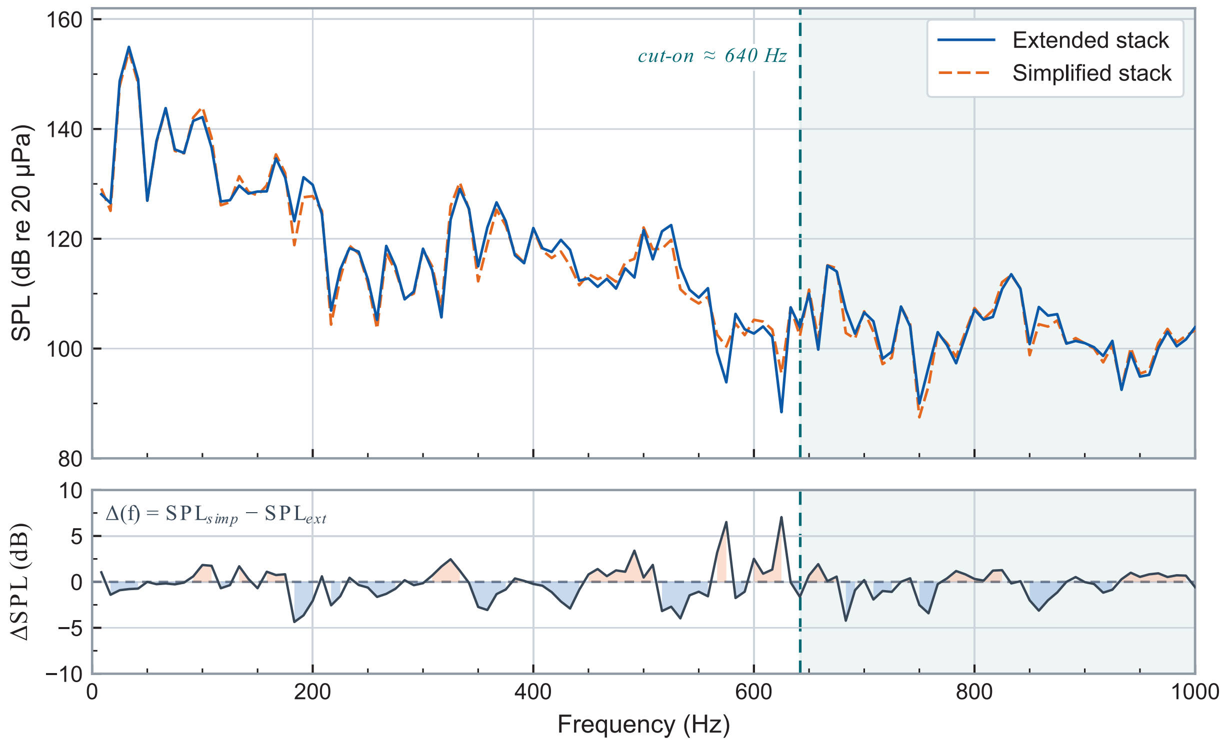

Fig. 9. Effect of the downstream exhaust-stack representation on the predicted post-turbine in-duct SPL at Location 1 (Fig. 4), comparing the simplified and explicit-stack configurations and their signed difference over 0–1000 Hz.

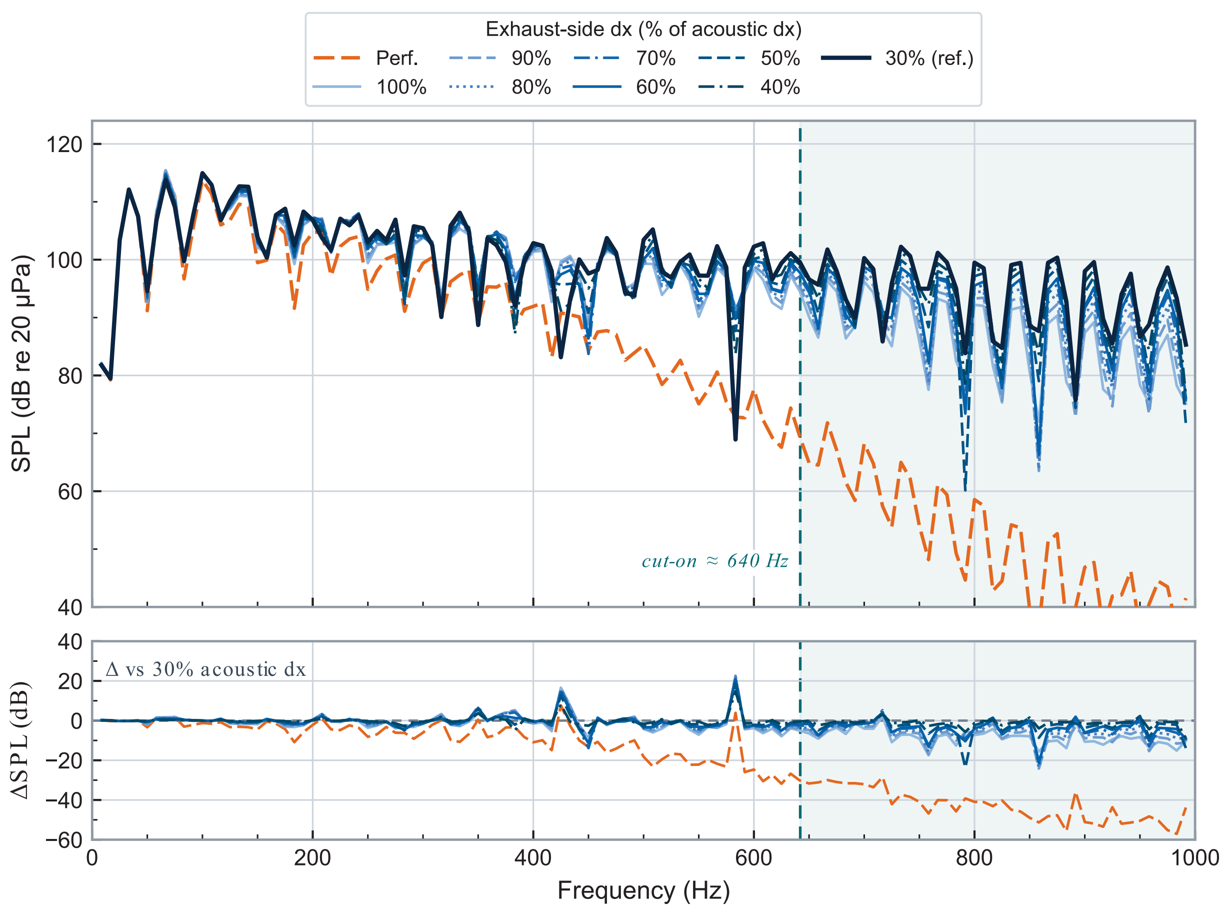

Fig. 10. Effect of exhaust-side discretization (dX) on the predicted free-field SPL at 100 % load. Top: spectra for the performance-oriented mesh and successive acoustic refinements (% of acoustic dX); bottom: signed difference relative to the 30 % acoustic dX reference.

phase redistribution, and distributed attenuation in the intervening duct network [8,31]. As a result, the immediate post-turbine in-duct response preserves nearly the same dominant spectral structure in both configurations, while the downstream stack still produces a secondary frequency-dependent reshaping of the local spectrum through reflection and interference effects [28]. These results indicate that, for the present configuration, explicit representation of the downstream exhaust stack is far more important for predicting the radiated free-field response than for predicting the in-duct SPL immediately downstream of the turbine.

3.3. Effect of discretization length (dX) on the engine exhaust acoustic characteristics

The sensitivity of the predicted SPL to the prescribed one-dimensional discretization length, *dX*, is evaluated by refining the exhaust and intake meshes separately. Because the conservation equations are integrated explicitly, the stable time step is adjusted concurrently according to the local Courant–Friedrichs–Lewy condition [24]. The investigated cases therefore constitute coupled spatial and CFL-controlled temporal refinements. The numerical scheme, combustion-model formulation, boundary conditions, friction and heat-transfer closures, and engine operating point are otherwise retained without retuning. Figs. 10–14 summarize the resulting changes using SPL overlays and signed spectral differences relative to the finest discretization adopted as the numerical reference.

A practical interpretation follows directly from wavelength-based resolution criteria for wave-propagation problems: resolving the shortest wavelength of interest typically requires *dX* to be well below the acoustic wavelength (often expressed as $dX \lesssim \lambda/10$ for low phase error) [24]. For exhaust-gas sound speeds on the order of 400–500 m/s, λ at 1 kHz is 0.4–0.5 m, implying *dX* on the order of 40–50 mm to avoid mesh-driven distortion, substantially finer than performance-oriented

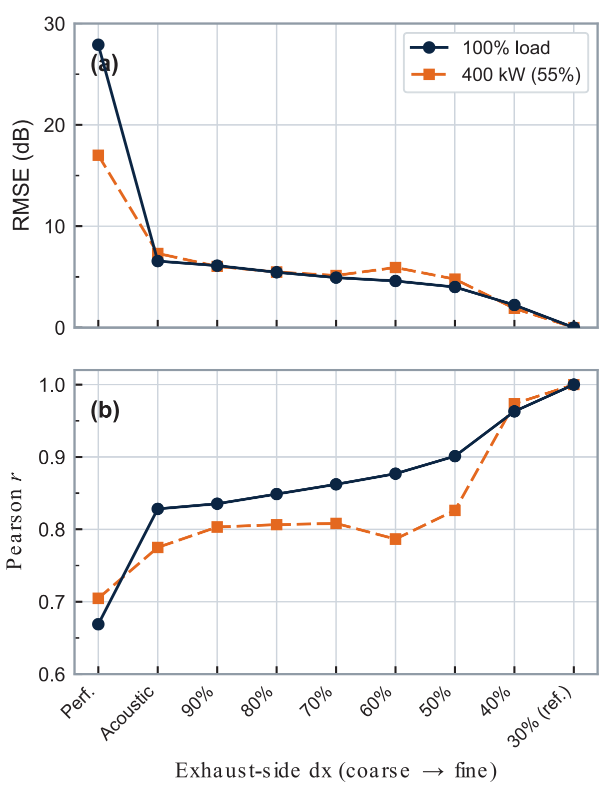

Fig. 11. Exhaust-side discretization convergence at two engine loads (1000 rpm at 100 % load and 1000 rpm at 400 kW (≈ 55 % load)): (a) RMSE and (b) Pearson correlation *r* versus mesh refinement, evaluated over 0–1000 Hz relative to the finest 30 % acoustic *dX* mesh.

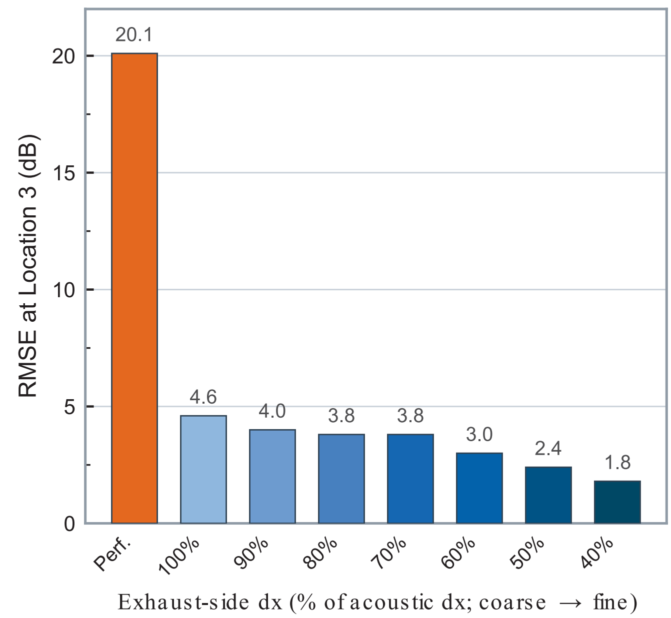

Fig. 12. RMSE of the predicted in-duct SPL at Location 3 for different exhaust-side discretization cases at 100 % load, using the 30 % acoustic *dX* case as the numerical reference. Bar labels indicate the RMSE values in dB.

settings. Quantitative metrics confirm this behavior. Relative to the finest exhaust reference (30 % acoustic *dX*), the performance-oriented mesh yields poor agreement (r ≈ 0.67, RMSE ≈ 27.9 dB), with only about 29 % of frequency points within ± 5 dB. As *dX* is reduced into the acoustically refined range, the solution converges steadily: for the 60 % and 50 % acoustic *dX* cases, the correlation rises from r ≈ 0.88 to 0.90, and the deviation falls from RMSE ≈ 4.59 to 4.00 dB, while the 40 % acoustic *dX* further improves agreement to r ≈ 0.96, RMSE ≈ 2.23 dB, with about 97 % of points within ± 5 dB. Restricting the comparison to the conservative subset at or below 600 Hz leaves this conclusion unchanged but tightens it: the large performance-mesh error decreases from RMSE ≈ 27.9 dB over 0–1000 Hz to ≈ 10.7 dB below 600 Hz, confirming that most of the coarse-mesh deviation originates above the cut-on frequency, in the band interpreted here only as an equivalent plane-wave trend. The remaining discrepancies are mainly frequency-local (small shifts in peak/notch location and depth), which is expected in a multi-branch exhaust network where even small residual phase errors can relocate interference features without changing the broadband envelope [41].

To verify that the discretization conclusion is not specific to the worst-case load, campaign C1 is repeated at the validation operating point (1000 rpm and 400 kW, ≈ 55 % load), using the same mesh levels and the same finest-mesh reference. As summarized in Fig. 11 and Table 6, the convergence behavior is essentially identical at both loads: the performance-oriented mesh is strongly inaccurate, agreement generally improves with refinement, and near-convergence is reached for the 40 % acoustic *dX* case (r ≈ 0.97, RMSE ≈ 1.9 dB at 55 % load). The absolute deviation of the coarse mesh is smaller at part load (RMSE ≈ 17.0 dB versus 27.9 dB at full load), reflecting the lower excitation amplitude and exhaust temperature; however, the ranking of the mesh levels and the rate of convergence are preserved. This confirms that coupled exhaust-side spatial and CFL-controlled temporal discretization remains the first-order numerical requirement across the investigated load range, and that the refined mesh selected for the model-to-measurement validation retains adequate resolution at the cooler part-load condition, where the shorter wavelengths impose a marginally stricter $dX \leq \lambda/10$ criterion.

The same trend is observed in the in-duct noise at Location 3, where progressive exhaust-side mesh refinement consistently reduces the

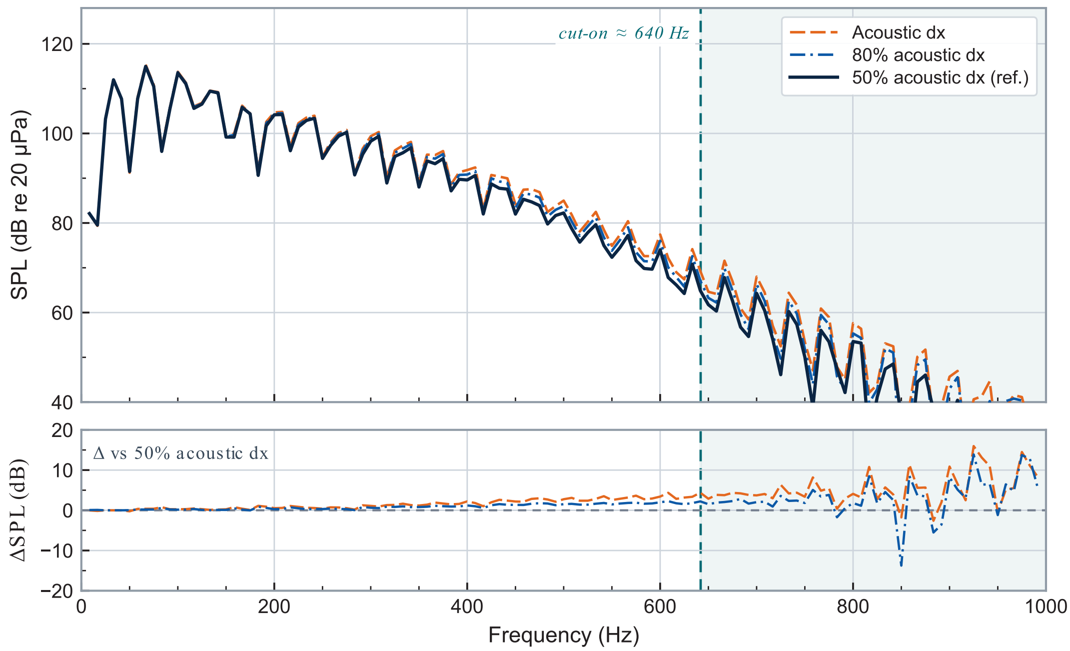

Fig. 13. Effect of intake-side discretization (dX) on the predicted free-field exhaust SPL at 100 % load. Top: spectra; bottom: signed difference relative to the 50 % acoustic dX reference.

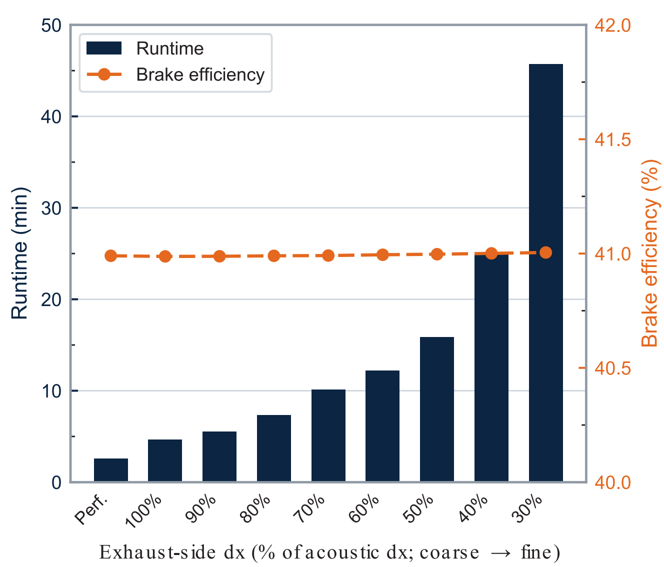

Fig. 14. Computational runtime and brake efficiency as a function of exhaust-side discretization length (dX), at 1000 rpm and 100 % load, illustrating the accuracy–cost trade-off of mesh refinement.

RMSE relative to the 30 % acoustic dX reference, as shown in Fig. 12.

In contrast, refining the intake-side dX produces only minor changes in the predicted free-field exhaust SPL (Fig. 13). The spectra remain strongly correlated with the finest intake reference ($r \approx 0.99$), and the differences become noticeable mainly at the upper end of the analyzed band, where spatial sampling demands are highest. This limited intake sensitivity, combined with the strong exhaust sensitivity in Fig. 10, indicates that the dominant discretization error in the predicted exhaust noise originates from wave-resolution quality in the exhaust network, not from intake mesh settings. The result is also consistent with the expected intake–exhaust acoustic decoupling across the turbocharger and valve system, which imposes strong impedance mismatches and limits cross-system wave transmission under the present conditions [42].

Table 6
Discretization convergence metrics (Pearson r and RMSE relative to the finest 30 % acoustic dX mesh) at 100 % and 55 % load, for the full band (0–1000 Hz) and the below-cut-on band (≤ 600 Hz).

Mesh	100 % load: full band	100 % load: ≤ 600 Hz	55 % load: full band	55 % load: ≤ 600 Hz
	r / RMSE (dB)	r / RMSE (dB)	r / RMSE (dB)	r / RMSE (dB)
Performance	0.67 / 27.9	0.71 / 10.7	0.71 / 17.0	0.63 / 13.3
Acoustic	0.83 / 6.6	0.85 / 4.3	0.78 / 7.3	0.78 / 5.2
90 % acoustic	0.84 / 6.1	0.85 / 4.2	0.80 / 6.0	0.79 / 5.0
80 % acoustic	0.85 / 5.5	0.86 / 4.1	0.81 / 5.5	0.80 / 5.0
70 % acoustic	0.86 / 4.9	0.86 / 4.1	0.81 / 5.1	0.80 / 4.9
60 % acoustic	0.88 / 4.6	0.88 / 3.8	0.79 / 5.9	0.84 / 4.3
50 % acoustic	0.90 / 4.0	0.92 / 3.2	0.83 / 4.8	0.86 / 4.0
40 % acoustic	0.96 / 2.2	0.96 / 2.3	0.97 / 1.9	0.98 / 1.5
30 % acoustic (ref)	1.00 / 0.00	1.00 / 0.00	1.00 / 0.00	1.00 / 0.00

Fig. 14 shows the computational consequence of refinement. Accordingly, runtime rises sharply as dX decreases. At the same time, brake efficiency remains essentially unchanged across the dX sweep, confirming that the operating point is not altered by the change in discretization length. Therefore, the SPL differences are attributed to numerical wave-resolution effects arising from the coupled spatial and CFL-controlled temporal refinement, rather than to changes in the engine operating state. Overall, the results indicate that the exhaust-side discretization must be sufficiently fine to prevent mesh-driven broadband bias and preserve peak–notch structure, while refinement beyond the near-converged range yields diminishing acoustic benefit relative to the rapidly increasing computational cost.

To interpret the observed discretization sensitivity independently of the software implementation, the coupled spatial and temporal resolution can be expressed through the CFL stability condition and the number of control volumes per acoustic wavelength. For an explicit time-domain solution of the quasi-one-dimensional conservation equations, the stable time step is constrained by the local Courant–Friedrichs–Lewy condition [24]:

$$\Delta t \leq C_{\mathrm{CFL}} \min_{j} \left(\frac{dX_j}{|u_j| + c_j} \right), \tag{14}$$

In Eq. (14), C_{CFL} is the prescribed Courant number, and dX_j, u_j, and c_j are the control-volume length, local axial gas velocity, and local speed of sound in control volume j, respectively. Reducing dX therefore also reduces the maximum stable time step. Consequently, the present sweep changes spatial and CFL-controlled temporal resolution concurrently. The CFL condition constrains numerical stability but does not, by itself, guarantee accurate wave propagation [24].

Spatial wave-propagation accuracy also depends on the number of control volumes used to represent the acoustic wavelength:

$$N_{\lambda} = \frac{\lambda}{dX} \approx \frac{c}{fdX} \tag{15}$$

Eq. (15) provides a nominal stationary-medium estimate. In subsonic mean flow, the downstream- and upstream-travelling wavelengths are modified approximately to $\lambda^{\pm} = (c \pm \overline{u})/f$ [36]. The commonly used criterion $N_{\lambda} \geq 10$ is therefore a practical engineering guideline rather than a universal convergence condition because the required resolution depends on the numerical scheme, time step, mean flow, and acceptable phase and amplitude errors [24,41].

The corresponding nominal screening frequency is $f_{10} \approx c/(10dX)$. For the relevant exhaust-gas sound-speed range of 400–500 m/s, the performance-oriented mesh (dX = 110 mm) gives $f_{10} \approx 364$–455 Hz, whereas the 40 % acoustic mesh selected for validation (dX = 22 mm) gives $f_{10} \approx 1.82-2.27$ kHz. These values are not sharp frequency limits because temperature, mean flow, control-volume length and numerical dispersion vary throughout the exhaust network. Nevertheless, they are consistent with the concentration of the coarse-mesh discrepancies toward the upper part of the spectrum and with the reduction in RMSE from approximately 27.9 dB over 0–1000 Hz to 10.7 dB over the conservative $f \leq 600$ Hz subset.

Table 7 quantifies the coupled spatial–temporal refinement. Reducing the exhaust-side dX from 110 to 16.5 mm increases the total number of control volumes from 530 to 3,046 and reduces the CFL-controlled time step from 60.5 to 16.3 µs. Both changes contributed to the increase in computational time shown in Fig. 14. The numerical scheme, physical closures, boundary conditions, and engine operating point are retained without retuning. The observed convergence therefore reflects coupled spatial and CFL-controlled temporal refinement, whose individual contributions cannot be separated within the present sweep.

These resolution requirements are especially non-trivial in a large-bore exhaust system. The concentration of acoustic energy at low firing orders might initially suggest that a performance-oriented coarse mesh is sufficient because the corresponding wavelengths are long. In practice, however, the long propagation path and multiple reflection sites allow small local phase errors to accumulate and shift the predicted peak–notch pattern [24,36]. Moreover, the local speed of sound varies substantially along the thermally non-uniform exhaust path [7]. Cooler regions shorten the local wavelength and therefore tighten the spatial-resolution requirement, whereas regions with high sound speed or flow velocity can control the CFL-limited time step [24]. The large exhaust-duct diameter imposes a separate physical constraint by lowering the first transverse-mode cut-on frequency; consequently, axial mesh refinement cannot recover the non-planar acoustic content above cut-on [36]. Acoustic suitability therefore cannot be inferred from a bore-scaled dX value alone. It must be established through coupled mesh/time-step convergence based on the minimum local convected wavelength, together with an independent assessment of the plane-wave-valid frequency range.

Table 7
Coupled spatial–temporal discretization sweep at 1000 rpm and 100 % load: exhaust-side dX, total control-volume count, CFL-controlled time step, and time steps per 720° CA engine cycle.

Mesh	Exhaust dX (mm)	Total control volumes	CFL-controlled time step (µs)	Time steps per 720° CA cycle
Performance	110	530	60.5	1,984
Acoustic	55	971	54.5	2,201
90 %	49.5	1,058	50.0	2,397
80 %	44.0	1,197	42.7	2,810
70 %	38.5	1,357	37.2	3,231
60 %	33.0	1,565	29.5	4,067
50 %	27.5	1,860	26.8	4,460
40 %	22.0	2,311	21.3	5,607
30 % (ref)	16.5	3,046	16.3	7,371

3.4. Effect of exhaust-volume tuning on the engine exhaust acoustic results

Figs. 15 and 16 compare the predicted free-field narrowband SPL obtained by varying the geometry of the selected upstream exhaust pipe section. Varying the pipe length produces only small, predominantly frequency-local changes (Fig. 15). The spectral shape remains close to the reference (r = 0.98 for + 20 % length and r = 0.97 for − 20 % length), with minor band-averaged level shifts (mean ΔSPL = − 0.46 dB and + 0.23 dB) and limited deviation (RMSE ≈ 2.35–2.36 dB). The SPL curves show slight relocation of peaks and dips rather than a systematic reduction, which is consistent with a duct-network response in which changing length primarily modifies phase accumulation and therefore the resonance/anti-resonance pattern (standing-wave/interference tuning) without strongly altering the overall transmission level [8,43].

Changing the pipe diameter yields a markedly stronger and more broadband response (Fig. 16). Compared with the reference, the + 20 % diameter case gives a mean ΔSPL of − 3.29 dB **(**RMSE = 4.34 dB, r = 0.97**)**, while the − 20 % diameter case gives a mean ΔSPL of − 4.28 dB **(**RMSE = 5.11 dB, r = 0.98**)**. The high correlations indicate that the dominant spectral structure is preserved, but the baseline is shifted downward much more consistently than in the length sweep.

Changing the pipe diameter changes its cross-sectional area according to $A \propto D^2$ and therefore changes the characteristic acoustic impedance $Z_c = \rho c/A$. If the local values of ρ and c are assumed to remain approximately unchanged across the area transition, the magnitude of the pressure-reflection coefficient can be estimated as $|R| = \frac{|A_1 - A_2|}{A_1 + A_2}$. For the + 20 % diameter case, $A_2/A_1 = 1.2^2 = 1.44$, giving $|R| = |1-1.44|/(1+1.44) \approx 0.18$. For the − 20 % diameter case, $A_2/A_1 = 0.8^2 = 0.64$, giving $|R| = |1-0.64|/(1+0.64) \approx 0.22$. The slightly larger idealized reflection estimate for the smaller-diameter case is consistent with, but does not uniquely explain, its larger predicted SPL reduction. Because the geometry varied within the coupled gas-dynamic model, the response may also include changes in local velocity, thermodynamic state, and distributed losses, together with multiple reflections and phase-dependent interference. Fig. 16 is therefore interpreted as a coupled thermo-fluid–acoustic sensitivity [8,31].

The same behavior is obtained at the 400 kW (55 %) validation load (Table 8): length variations again produce negligible level changes (|mean ΔSPL| ≤ 0.8 dB), while ± 20 % diameter variations give consistent broadband reductions of about 5 dB, confirming that the dominance of area-over-length-related effects is not specific to full load.

3.5. Effect of the flow-split geometry variation on the engine exhaust acoustic simulation results

Fig. 17 shows the effect of varying the flow-split characteristic length by ± 20 % relative to the reference configuration. The predicted free-field SPL is essentially unchanged over the full analyzed range. The differences remain very small for both the + 20 % case (mean ΔSPL = +0.04 dB, RMSE = 0.33 dB, r = 0.999) and the − 20 % case (mean ΔSPL

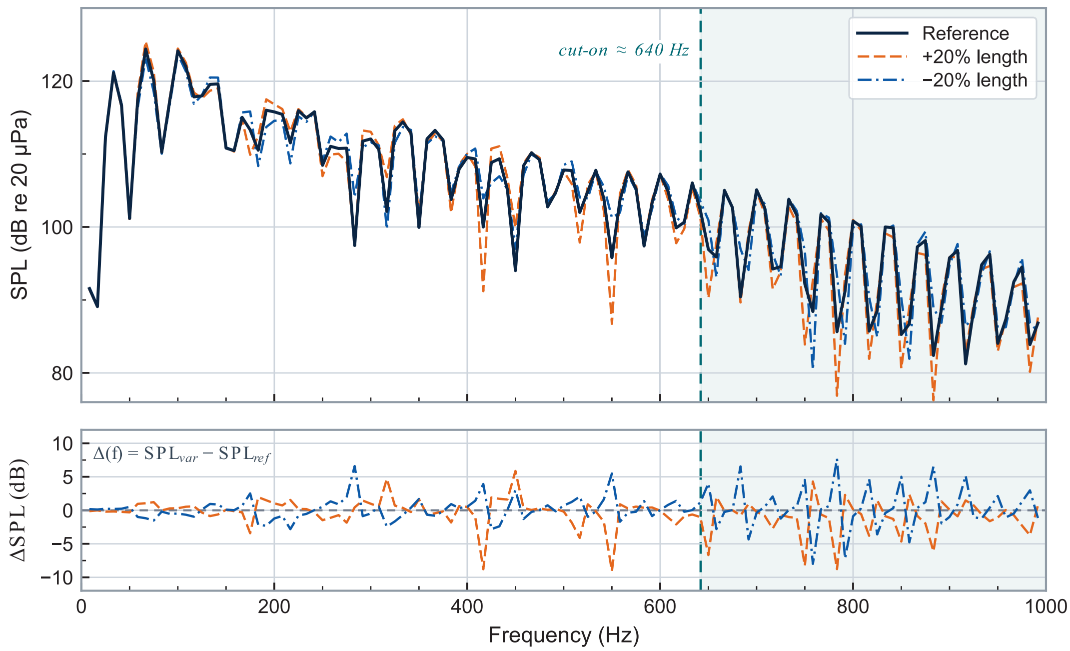

Fig. 15. Effect of upstream exhaust-pipe length variation (±20 %) on the predicted free-field SPL, relative to the reference geometry (1000 rpm, 100 % load). Top: spectra; bottom: ΔSPL.

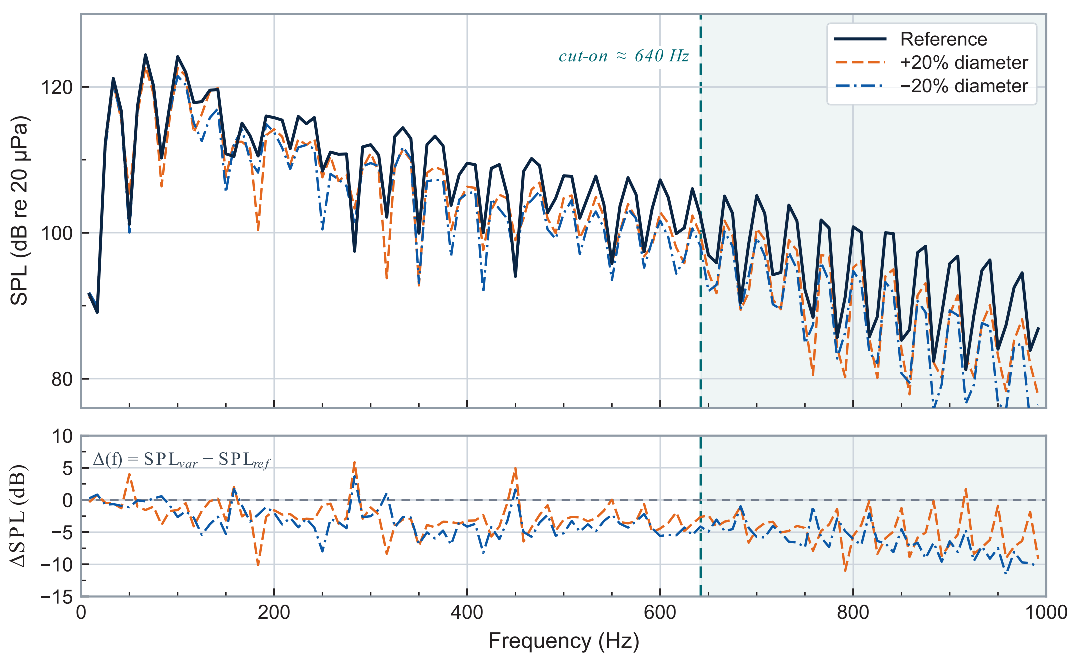

Fig. 16. Effect of upstream exhaust-pipe diameter variation (±20 %) on the predicted free-field SPL, relative to the reference geometry (1000 rpm, 100 % load). Top: spectra; bottom: ΔSPL.

Table 8
Exhaust-volume sensitivity: mean ΔSPL, RMSE, and r relative to the reference geometry, for ± 20 % length and diameter at 100 % and 55 % load (0–1000 Hz).

Variation	100 % load: mean ΔSPL (dB) / RMSE (dB) / r	55 % load: mean ΔSPL (dB) / RMSE (dB) / r
+20 % length	−0.46 / 2.35 / 0.98	+0.77 / 3.86 / 0.95
−20 % length	+0.23 / 2.36 / 0.97	−0.14 / 2.45 / 0.98
+20 % diameter	−3.29 / 4.34 / 0.97	−5.14 / 6.71 / 0.95
−20 % diameter	−4.28 / 5.11 / 0.98	−4.89 / 6.22 / 0.96

= − 0.13 dB, RMSE = 0.54 dB, r = 0.999), with the corresponding ΔSPL curves staying close to zero across the band. This indicates that, for the present junction configuration, characteristic length is not a sensitive acoustic control parameter. Its influence is limited to a small local phase adjustment inside the junction model, which is too weak to materially change the reflection/transmission balance or the overall acoustic energy reaching the outlet. By contrast, varying the flow-split expansion diameter produces a reduction in the predicted free-field SPL, as shown in Fig. 18. The + 20 % diameter case yields an average change of − 2.71 dB relative to the reference, whereas the − 20 % case gives a larger mean reduction of − 4.52 dB. In both cases, the attenuation becomes more

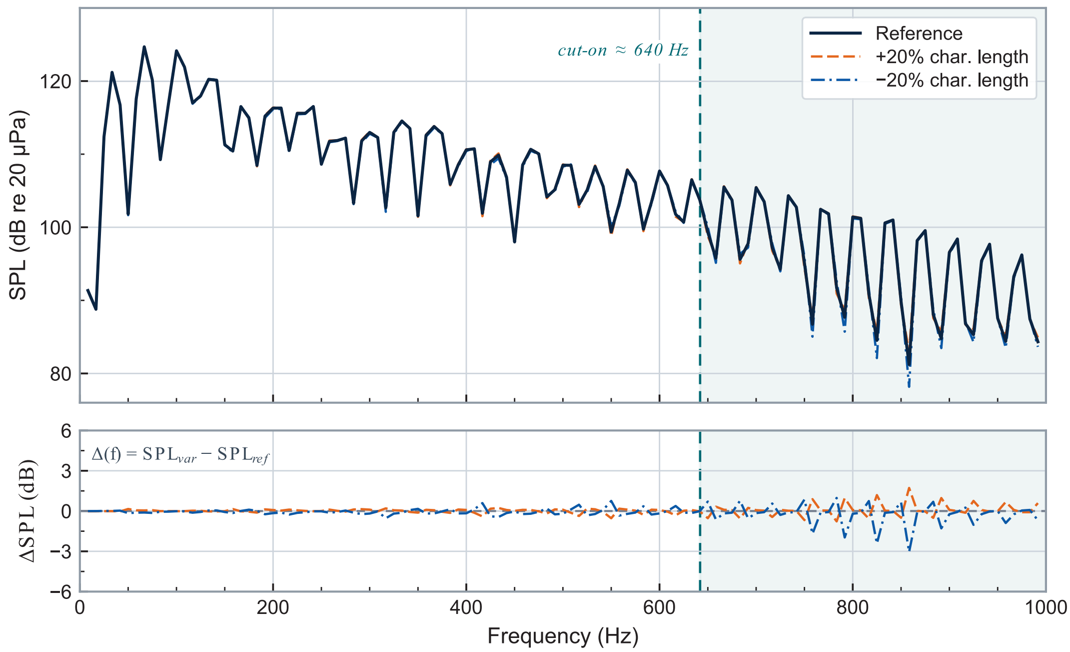

Fig. 17. Effect of flow-split characteristic length (±20 %) on the predicted free-field SPL, relative to the reference configuration (1000 rpm, 100 % load). Top: spectra; bottom: ΔSPL.

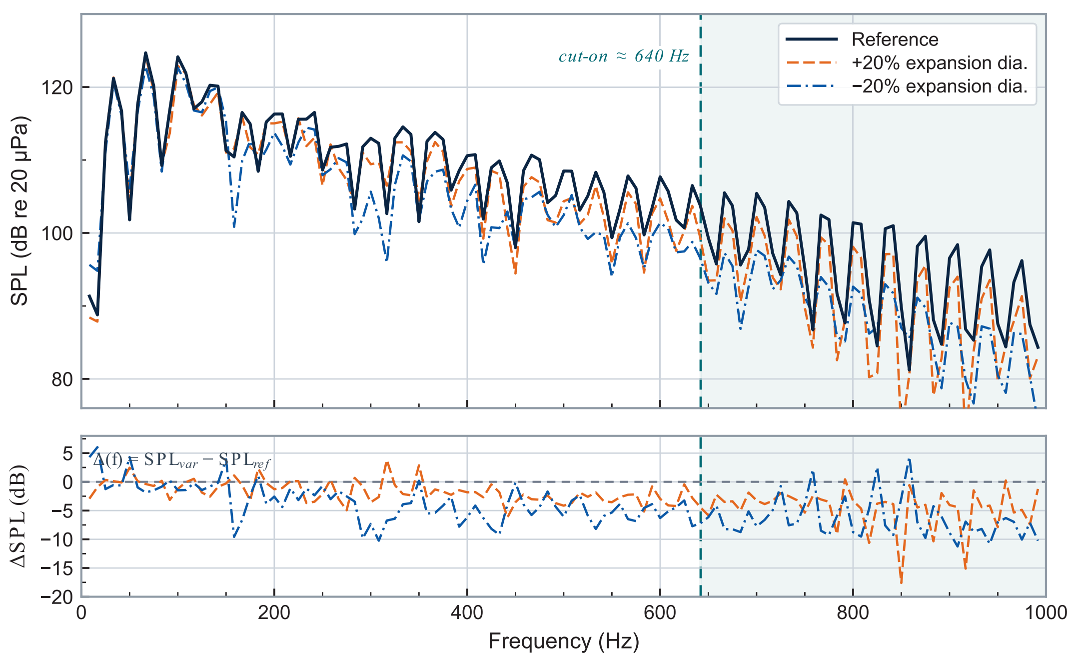

Fig. 18. Effect of flow-split expansion diameter (±20 %) on the predicted free-field SPL, relative to the reference configuration (1000 rpm, 100 % load). Top: spectra; bottom: ΔSPL.

pronounced toward the upper part of the analyzed band, where the Δ SPL curves remain predominantly negative.

The physical reason is analogous to the stronger sensitivity already observed for pipe-diameter variation in the previous section. Changing the expansion diameter modifies the local cross-sectional area of one section embedded within an otherwise connected pipe network. This creates stronger area discontinuities at the interfaces of the modified section and therefore changes the local characteristic impedance seen by incident waves. As a result, the reflection–transmission balance at the flow split is altered: a smaller fraction of the incident wave energy is transmitted into the downstream branch, while a larger fraction is reflected or redistributed among the connected branches, thereby reshaping the interference field throughout the branched duct system. These area-driven junction effects are inherently frequency-dependent because the effective impedance of the junction depends not only on the local area ratios but also on the dynamic acoustic loading and resonance states of the connected branches [8,27]. An important feature observed in Fig. 18 is that perturbing the expansion diameter always reduces the radiated SPL, with the contraction case producing the stronger effect. This indicates that the reference configuration is closer to a locally better-matched transmission state for this network, while changing the diameter in either direction increases the impedance mismatch and consequently modifies the reflection and redistribution of acoustic energy.

The same behavior is confirmed at the 400 kW (55 %) load: characteristic-length variations remain small, while expansion-diameter variations again produce the dominant reductions, with the contraction (−20 %) case strongest at both loads. This confirms that the junction acoustic response is governed by area-related impedance change rather than characteristic length across the investigated load range.

3.6. Effect of the turbocharger acoustic representation on the exhaust-pressure spectra

To isolate turbocharger-model effects from downstream duct tuning, this comparison is performed with the simplified exhaust layout, so the observed differences mainly reflect changes in passive transmission/reflection and in the effective acoustic boundary conditions imposed by the turbocharger models.

Fig. 19 shows that replacing the map-based compressor representation with the geometry-based reduced-order model does not produce systematic broadband attenuation in the predicted exhaust SPL over 0–1000 Hz. Instead, the changes appear mainly as (i) small frequency shifts of existing features and (ii) changes in peak levels and notch depths, most clearly above approximately 300 Hz. A physically consistent interpretation in a 1D network is that the discretized compressor modifies the intake-side acoustic impedance and introduces a more realistic distributed geometry (volute/area variation), which changes the reflection phase and the frequency-dependent filtering of pressure waves in the intake path. Those intake-side changes couple into the exhaust spectrum primarily through the gas-exchange process (valve overlap and cylinder filling/emptying), where small phase changes in the intake wave field can retune the timing and spectral content of the cylinder discharge, which then excites the turbine inlet. The consequence is exactly what Fig. 19 shows: feature relocation (frequency shift) and reshaping (peak/notch magnitude changes), without a broadband level drop [8,26].

Fig. 20 exhibits a stronger and qualitatively different response. Replacing the map-based turbine with the acoustic turbine model reduces the radiated SPL across most of the 0–1000 Hz range, with attenuation increasing toward higher frequencies. The accompanying numerically calculated transmission-loss (TL) curve provides a model-consistent interpretation at this 100 % load condition: the map-based turbine exhibits a low, nearly frequency-independent TL (∼4 dB), whereas the acoustic turbine develops a strongly frequency-dependent TL that rises from ∼ 2–3 dB at low frequency to ∼ 15–17 dB near 1 kHz; above ∼ 150 Hz it exceeds the map-based value, progressively reducing the transmitted wave energy toward higher frequencies. This behavior is consistent with the reduced-order turbine acting as a frequency-dependent acoustic two-port: its equivalent ducts, lumped volume, and cross-sectional transitions introduce acoustic storage, phase accumulation, and impedance discontinuities that modify wave reflection and transmission under pulsating flow. Comparable TL magnitudes and their dependence on operating conditions are reported in two-port-based turbine acoustic characterizations [27].

The consistency of the mean operating point is verified to ensure that the observed acoustic changes stem from passive wave transmission rather than from a shifted operating condition. At 1000 rpm and 25 bar BMEP (unchanged between the two models), the map-based and acoustic turbine models yield closely matched turbine conditions: the turbine-inlet pressure changes only marginally, from 3.51 to 3.55 bar, and the outlet pressure from 1.015 to 1.04 bar, giving a nearly identical expansion ratio (≈3.46 vs ≈3.41). The inlet and outlet temperatures likewise remain close, at 809 → 802 K and 630 → 635 K, respectively. The mass flow after the turbine changes from 1617 to 1610 g/s, which shows a minor difference. These small differences confirm that the acoustic turbine substitution preserves the mean engine operating state while introducing the intended passive wave-transmission and reflection behavior.

Overall, the results demonstrate that turbocharger modeling fidelity strongly affects predicted exhaust noise, even when operating conditions and steady-state engine performance remain unchanged. While the acoustic compressor primarily redistributes spectral content through phase and impedance effects, the acoustic turbine serves as an effective passive acoustic filter that significantly attenuates the transmission of pressure waves. These findings highlight that map-based turbocharger representations, although adequate for performance simulations, can significantly under-represent turbine acoustic attenuation and thereby bias exhaust noise predictions if passive acoustic behavior is not properly modeled.

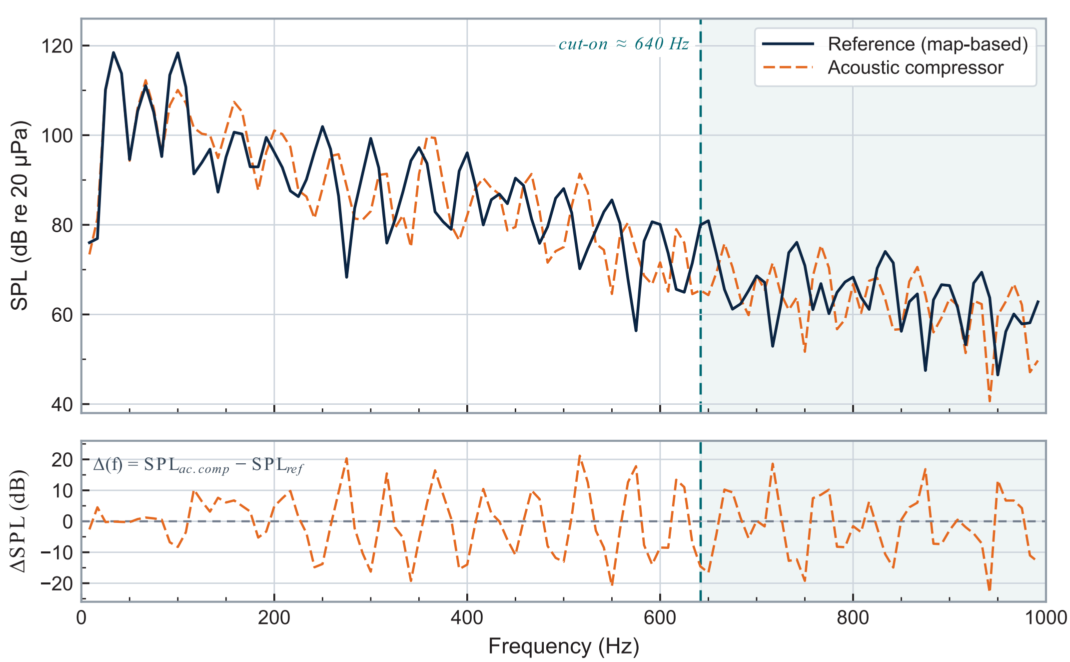

Fig. 19. Predicted free-field SPL with the reference (map-based) turbocharger and the discretized acoustic compressor model (1000 rpm, 100 % load, simplified exhaust).

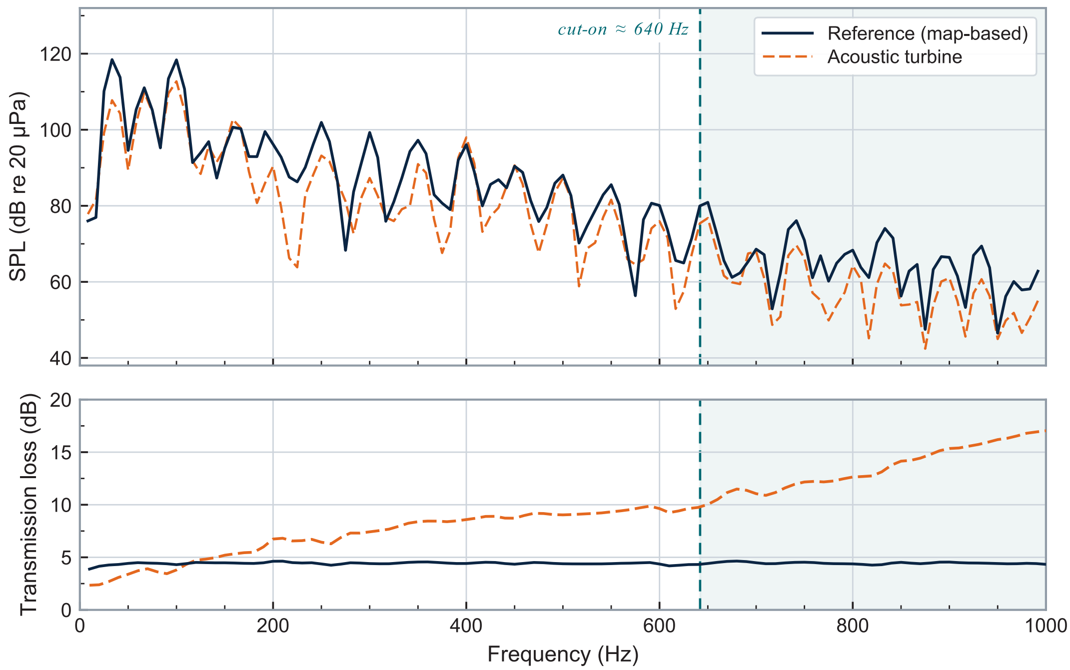

Fig. 20. Effect of turbine acoustic modeling on the predicted free-field SPL (top) and the corresponding turbine transmission loss (bottom), for the reference map-based and acoustic turbine models (1000 rpm, 100 % load, simplified exhaust).

3.7. Experimental assessment of the sensitivity-guided model refinement

Based on the preceding sensitivity results, the refined model combines coupled exhaust-side spatial and CFL-controlled temporal refinement, a passive acoustic turbine representation, and explicit downstream-stack geometry. These modifications address numerical wave resolution, turbine acoustic transmission, and downstream propagation, respectively. Because dX and Δt change together and all three modifications are implemented simultaneously, each configuration is evaluated as a complete system through its deviation from measurement; the contribution of any individual modification cannot be isolated from the final validation.

Validation is based only on the in-duct measurements, because the computational model omits the silencers and after-treatment components needed for absolute free-field comparison. Table 9 defines the final model settings. Fig. 21 evaluates the simplified and refined configurations separately against the same measurement at Location 1, while Location 3 provides a separate comparison of the refined prediction with the local downstream measurement.

At Location 1, the simplified and refined predictions were evaluated separately against the same measured spectrum. The narrowband model–measurement MAE is 9.66 ± 1.12 dB for the simplified configuration and 7.57 ± 1.06 dB for the refined configuration. The corresponding RMSE values are 11.42 and 9.88 dB, the bias-removed RMSE values are 11.16 and 9.40 dB, and the one-third-octave RMSE values are 8.19 and 6.81 dB, while r is 0.736 and 0.764, respectively. The consistently smaller frequency-resolved deviations and slightly higher correlation indicate closer reproduction of the measured spectral pattern by the refined configuration, rather than only a change in its mean level. Its MAE is lower against each of the 87 measured cycles, with a mean paired difference of 1.95 dB and an empirical 2.5–97.5 percentile range of 1.50–2.37 dB. At the individual-frequency level, the absolute deviation from measurement is smaller at 43 of the 76 evaluated frequencies, showing that the closer agreement is distributed across much of the spectrum but is not uniform at every frequency.

The mean-level result provides an important qualification. The measured arithmetic mean of the 76 line levels is 122.48 ± 1.3 dB, whereas the simplified and refined predictions are 120.05 and 119.42 dB. The corresponding absolute model–measurement deviations are 2.42 and 3.05 dB, while the firing-order MAE values are 5.29 and 5.70 dB for the simplified and refined configurations, respectively. Thus, the refined configuration more closely reproduces the overall peak–notch pattern but does not provide smaller deviations in the mean level or the selected firing harmonics. This mixed response is physically consistent with the sensitivity analysis. Reducing dX from 110 to 22 mm places the complete below-cut-on band within the nominal ten-cells-per-wavelength range, while the accompanying CFL-controlled time step limits temporal discretization error. Together, these changes reduce numerical dispersion and the accumulation of phase error between reflection sites [24,41].

At the same time, the passive turbine develops greater transmission loss than the map-based element above approximately 150 Hz, which tends to reduce the pressure level immediately downstream of the turbine. Because the simplified model already underpredicts the measured mean at Location 1, this additional attenuation moves the mean level in the unfavorable direction even as improved wave resolution and stack representation improve spectral shape. The transmission-loss comparison was obtained at the 100 % load sensitivity condition, so it supports the direction of this mechanism rather than quantifying its isolated contribution at the validation operating point.

Table 9
Final refined-model settings relative to the baseline.

Setting	Baseline	Refined model
Exhaust-side dX	110 mm	22 mm (40 % of the 55 mm acoustic-reference dX)
Intake-side dX	88 mm	44 mm (acoustic-reference dX)
Exhaust stack	Simplified (two pipes + flow restriction)	Explicit geometry — lengths, bends, junctions; no silencers
Turbine	Performance-map element only	Reduced-order acoustic representation: equivalent tongue and volute ducts, lumped rotor volume, performance-map element and expanding outlet duct
Junctions and exhaust volume	Reference	Reference (unchanged)

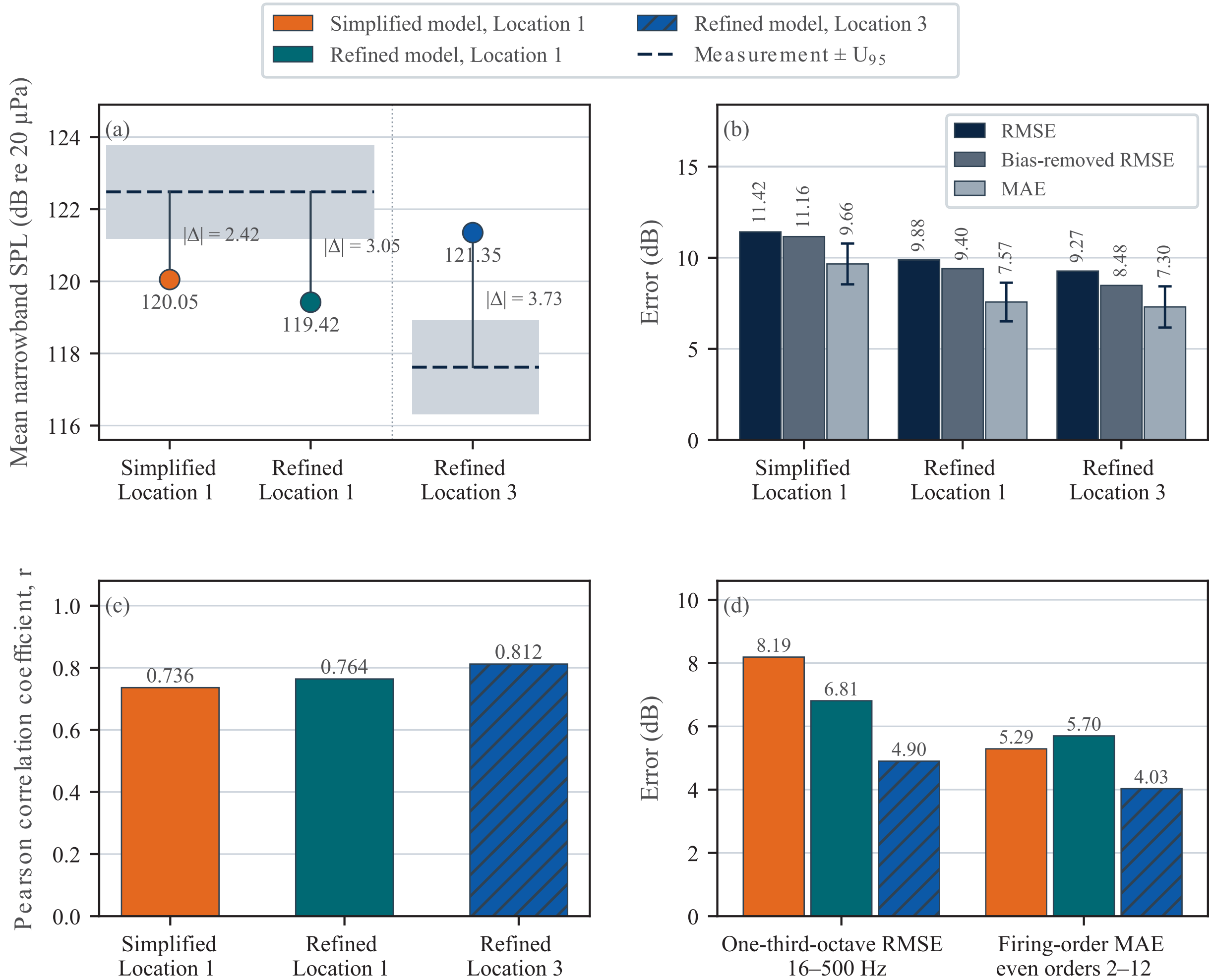

Fig. 21. Complete-cycle in-duct validation at 1000 rpm and 400 kW on the native 8.33 Hz grid over the 76 below-cut-on lines from 8.33 to 633.33 Hz. (a) Arithmetic mean narrowband SPL; dashed lines show the measured means and shaded bands their expanded uncertainty ($U_{95} = \pm 1.3$ dB, $k = 2$). (b) Narrowband RMSE, bias-removed RMSE, and MAE; MAE error bars show metric-specific expanded measurement uncertainty. (c) Pearson correlation coefficient. (d) One-third-octave RMSE and firing-order amplitude MAE at even orders 2–12. Measurement positions are defined in Fig. 2 and the corresponding model extraction points in Fig. 4.

At Location 3, comparison of the refined prediction with the local measurement gives a narrowband MAE of 7.30 ± 1.13 dB, an RMSE of 9.27 dB, a bias-removed RMSE of 8.48 dB, and $r = 0.812$. The corresponding one-third-octave RMSE and firing-order MAE are 4.90 and 4.03 dB, respectively. These values represent the smallest frequency-resolved errors among the three model–measurement evaluations shown in Fig. 21, although the mean-level deviation is not the smallest. The lower one-third-octave RMSE indicates smaller band-aggregated deviations, the lower firing-order MAE indicates closer agreement at the selected even firing harmonics, and the higher correlation indicates greater similarity in the relative narrowband variation. These metrics do not imply uniform agreement at every frequency. This behavior is physically consistent with the explicit pipeline providing a more realistic frequency-dependent acoustic transfer path: its propagation lengths determine phase accumulation, while its impedance discontinuities generate reflections and wave interference. Together, these effects govern the local peak–notch structure and firing-harmonic amplitudes at Location 3. However, because the simplified configuration has no corresponding Location 3 extraction plane, this result validates the complete refined configuration against the downstream measurement but does not demonstrate the isolated contribution of the pipeline.

Despite the comparatively smaller frequency-resolved errors at Location 3, the two measurement planes reveal a remaining deficiency in the predicted net propagation level. The measured arithmetic mean line level decreases by 4.86 dB between Locations 1 and 3, from 122.48 to 117.62 dB, whereas the refined model predicts an increase of 1.93 dB, from 119.42 to 121.35 dB. The resulting 6.79 dB discrepancy in the station-to-station change is less sensitive than either absolute level to an excitation error common to both planes. It therefore points toward deficiencies in the represented propagation path or downstream boundary, although it does not uniquely exclude excitation or other model-form errors.

Two mechanisms are consistent with the overpredicted downstream level. First, distributed attenuation may be underestimated. Wall friction and visco-thermal losses accumulate with frequency and propagation distance [31], while the modeled thermal state affects sound speed, density, viscosity, boundary-layer losses, and the phase accumulated along the stack [7]. Second, the ambient-pressure outlet boundary does not reproduce the frequency-dependent input impedance of the omitted silencers. Reflected waves can therefore alter the local standing-wave amplitude, particularly at Location 3, which lies approximately 8 m upstream of the first silencer compared with about 23 m for Location 1 [8,31]. The present measurements do not separate these contributions.

Interpretation is limited to the plane-wave range below the conservative 640 Hz cut-on frequency, and the reported uncertainty covers measurement-related variability rather than model-form or input uncertainty. Moreover, because the mesh, turbine, and downstream-geometry modifications were implemented together, their individual contributions cannot be isolated from the final validation. Within these limits, Fig. 21 shows closer frequency-resolved model–measurement agreement for the refined configuration at Location 1, despite the absence of smaller mean-level and firing-order deviations at that station. Location 3 provides the numerically strongest frequency-resolved agreement, including the lowest firing-order MAE. However, the incorrect station-to-station mean-level trend indicates that the representation of downstream net attenuation and termination impedance remains a key unresolved aspect of the model.

4. Conclusion

This study shows that improving exhaust-noise prediction in large-bore engines requires acoustic-focused modeling beyond conventional performance calibration. The principal findings can be summarized as follows:

- Mean-flow accuracy alone is insufficient for acoustic prediction. The baseline model reproduced the principal engine-performance quantities, yet its below-cut-on comparison with the measured post-turbine spectrum remained limited, confirming that the acoustic response is governed by unsteady wave propagation, reflection and phase interaction rather than by mean-flow agreement.
- Exhaust-side resolution is the first-order numerical requirement, and it is inseparably spatial and temporal because the Courant–Friedrichs–Lewy condition ties the time step to the mesh. Below 600 Hz, the performance-oriented mesh gave an RMSE of 10.7 dB relative to the finest-mesh reference, against 2.3 dB and $r = 0.96$ for the selected 40 % acoustic mesh.
- Downstream-system representation matters more than local geometry. Explicit stack modeling changed the mean free-field level by only 1.6 dB but produced a mean absolute spectral deviation of 8.2 dB, so a small level change can conceal substantial frequency-selective redistribution; by comparison, ±20 % duct-geometry variations gave frequency-local changes or broadband shifts of 3–5 dB. Because the local mean-flow and loss characteristics were not independently constrained, these geometry results are interpreted as coupled thermo-fluid–acoustic sensitivities. These free-field quantities are model-to-model indicators obtained under a compact-monopole approximation and were not validated against measurement.
- The turbine should be represented as a passive acoustic transmission element rather than solely as a steady-flow device. At the 100 % load sensitivity condition, the reduced-order representation yielded a numerically estimated TL that increased from approximately 2–3 dB at low frequencies to 15–17 dB near 1 kHz, whereas the map-based representation produced a nearly frequency-independent value of approximately 4 dB. The corresponding changes in the mean operating quantities were minor.
- Sensitivity-guided combined refinement produced generally smaller frequency-resolved discrepancies, although important limitations remain. Immediately downstream of the turbine, the narrowband MAE fell from 9.66 ± 1.12 to 7.57 ± 1.06 dB for all 87 measured cycles, the narrowband RMSE from 11.42 to 9.88 dB and the bias-removed RMSE from 11.16 to 9.40 dB, while r rose from 0.736 to 0.764. The mean-level deviation and the firing-order MAE moved the other way, from 2.42 to 3.05 dB and from 5.29 to 5.70 dB: refinement improves the resolved spectral pattern rather than the absolute level. A separate downstream comparison gave MAE = 7.30 ± 1.13 dB, RMSE = 9.27 dB and $r = 0.812$, yet the measured mean line level falls by 4.86 dB between the two stations while the model predicts a 1.93 dB rise, pointing to distributed attenuation, the modeled thermal state and the downstream boundary impedance without isolating their contributions. Residual narrowband errors of 9–10 dB remain the principal limitation, and no conclusion is drawn about frequency shifts smaller than the native 8.33 Hz Fourier spacing. Because the numerical, turbine, and downstream-network modifications were applied together, the observed changes cannot be attributed quantitatively to any individual refinement.

For the investigated engine and operating range, the results suggest a practical modeling sequence: establish wavelength-based numerical convergence first, then represent the downstream stack and passive turbine response, and examine local duct and junction geometry last. The transferable requirement is to resolve the relevant local wavelengths and represent the dominant impedance discontinuities, transmission elements and thermally dependent propagation paths, while the corresponding dX thresholds and component sensitivities remain platform-specific. Validation covered one engine platform and one measured acoustic condition, below cut-on, with silencers and aftertreatment omitted and the exterior sound field represented by a compact-monopole approximation. Downstream impedance and thermal state, silencer-induced reflections and the plane-wave assumption near cut-on remain plausible contributors to the residual errors and require further experimental assessment.

CRediT authorship contribution statement

Touraj Hashempour: Writing – review & editing, Writing – original draft, Visualization, Validation, Software, Methodology, Investigation, Formal analysis, Data curation, Conceptualization. **Jeyoung Kim:** Investigation. **Muhammad Danish Idrees:** Investigation. **Carlo Pestelli:** Methodology. **Zengxin Gao:** Methodology. **Maciej Mikulski:** Writing – review & editing, Project administration.

Declaration of competing interest

The authors declare the following financial interests/personal relationships which may be considered as potential competing interests: Touraj Hashempour reports financial support was provided by Business Finland. If there are other authors, they declare that they have no known competing financial interests or personal relationships that could have appeared to influence the work reported in this paper.

Acknowledgements

This work was carried out as part of the Silent Engine project (ref. 604/31/2022). The project was co-funded by Business Finland through NextGenerationEU funding. The authors gratefully acknowledge this support.

Data availability

Data will be made available on request.

References

[1] European Parliament and Council of the European Union, Directive 2000/14/EC of the European Parliament and of the Council of 8 May 2000 on the approximation of the laws of the Member States relating to the noise emission in the environment by equipment for use outdoors. 2000, pp. 1–78.
[2] European Parliament and Council of the European Union, "Directive 2002/49/EC of the European Parliament and of the Council of 25 June 2002 relating to the assessment and management of environmental noise," Brussels, 2002. Accessed: Apr. 29, 2026. [Online]. Available: https://eur-lex.europa.eu/legal-content/EN/TXT/?uri=CELEX:32002L0049.
[3] International Maritime Organization, "REVISED GUIDELINES FOR THE REDUCTION OF UNDERWATER RADIATED NOISE FROM SHIPPING TO ADDRESS ADVERSE IMPACTS ON MARINE LIFE," 2024. Accessed: Apr. 29, 2026. [Online]. Available: https://wwwcdn.imo.org/localresources/en/MediaCentre/Documents/MEPC.1-Circ.906-Rev.1%20-%20Revised%20Guidelines%20For%20The%20Reduction%20Of%20Underwater%20Radiated.pdf.
[4] International Maritime Organization, "RESOLUTION MSC.337(91) (adopted on 30 November 2012) CODE ON NOISE LEVELS ON BOARD SHIPS," 2014. Accessed: Apr. 29, 2026. [Online]. Available: https://wwwcdn.imo.org/localresources/en/KnowledgeCentre/IndexofIMOResolutions/MSCResolutions/MSC.337(91).pdf.
[5] Davies POAL, Holland KR. I.C. engine intake and exhaust noise assessment. J Sound Vibrat 1999;223(3):425–44. https://doi.org/10.1006/jsvi.1998.2093.

[6] Lee T-K, Joo W-H, Bae J-G. Exhaust noise control of marine diesel engine using hybrid silencer. Trans Korean Soc Noise Vib Eng 2009. https://doi.org/10.5050/KSNVN.2009.19.7.679.
[7] Seldon W, Shoeb A, Schimmel D, Cromas J. Experimental GT-POWER correlation techniques and best practices low frequency acoustic modeling of the exhaust system of a naturally aspirated engine. SAE Technical Papers, SAE International 2017. https://doi.org/10.4271/2017-01-1793.
[8] Munjal ML. Acoustics of ducts and mufflers. 2nd Edition. John Wiley & Sons; 2014.
[9] Cheng L, Jia Y-H, Li F-F, Qiu J. Cloud chamber experimental study for acoustic fog elimination technology. Appl Acoustics 2024;219:109885. https://doi.org/10.1016/j.apacoust.2024.109885.
[10] Li F-F, Jia Y-H, Wang G-Q, Qiu J. Mechanism of cloud droplet motion under sound wave actions. J Atmos Ocean Technol 2020;37(9):1539–50. https://doi.org/10.1175/JTECH-D-19-0210.1.
[11] Somashekarappa M. A noise reduction technique in internal combustion engines: a multidisciplinary approach. World J Adv Res Rev 2020;5(3):170–9. https://doi.org/10.30574/wjarr.2020.5.3.0012.
[12] Mikulski M, Ovaska T, Rabetino R, Kangasjärvi M, Myllykangas A. Clean Propulsion Technologies: Securing Technological Dominance for the Finnish Marine and Off-Road Powertrain Sectors. Energies 2025;18(5):1240. https://doi.org/10.3390/en18051240.
[13] Vasudev A, Soleimani A, Hyvönen J, Mikulski M. Feasible route towards decarbonising marine transport with flexible, hydrogen-enriched, reactivity controlled compression ignition mid-speed engines. Int J Hydrogen Energy 2025;142:1196–210. https://doi.org/10.1016/j.ijhydene.2025.02.152.
[14] Vasudev A, Mikulski M, Balakrishnan PR, Storm X, Hunicz J. Thermo-kinetic multi-zone modelling of low temperature combustion engines. Prog Energy Combust Sci 2022;91. https://doi.org/10.1016/j.pecs.2022.100998.
[15] Vasudev A, Kim J, Golbaghi K. A system-level simulation framework for developing next-generation marine gas engines. Appl Therm Eng 2026. https://doi.org/10.1016/j.applthermaleng.2026.131209. in press.
[16] Panda KC. Dealing with noise and vibration in automotive industry. Procedia Eng 2016;144:1167–74. https://doi.org/10.1016/j.proeng.2016.05.092.
[17] Dehner R, Sriganesh P, Selamet A, Miazgowicz K. Generation mechanism of broadband whoosh noise in an automotive turbocharger centrifugal compressor. J Turbomach 2021;143(12):Dec. https://doi.org/10.1115/1.4051274.
[18] Millo F, et al. Development of a numerical methodology for the assessment of flow noise in complex engine exhaust systems, 2021. doi: 10.4271/2021-01-1043.
[19] Kyaw Oo D'Amore G, Morgut M, Biot M, Mauro F, Kašpar J. Integration and optimization of the after-treatments systems to reduce the acoustic footprint of the ships. Appl Acoustics 2023;213:Oct. https://doi.org/10.1016/j.apacoust.2023.109625.
[20] Kong KJ. A 1D–3D approach for fast numerical analysis of the flow characteristics of a diesel engine exhaust gas. Machines 2021;9(10):Oct. https://doi.org/10.3390/machines9100239.
[21] Zheng S, Kang Z, Lian X. Acoustic simulation for exhaust silencer of vehicle engine with combined one/three-dimensional approach. Int J Vehicle Design 2012;60(2):57–70.
[22] Montenegro G, Onorati A, Fairbrother R. Modeling of silencers for internal combustion engines: 1D–3D coupling, network of 1D elements and a generic 3D cell approach. In: 9th International Conference on Engines and Vehicles; 2009. https://doi.org/10.4271/2009-24-0133.
[23] Mohamad BA. 1D and 3D modeling of modern automotive exhaust manifold. J Serbian Soc Comput Mech 2019;13(1):80–91. https://doi.org/10.24874/jsscm.2019.13.01.05.
[24] LeVeque RJ. Finite Volume Methods for Hyperbolic Problems. Cambridge: Cambridge University Press, 2002. doi: 10.1017/CBO9780511791253.
[25] "Acoustics Application Manual GT-SUITE," 2026. [Online]. Available: www.gtisoft.com.
[26] Serrano JR, Arnau FJ, Novella R, Reyes-Belmonte MÁ. A procedure to achieve 1D predictive modeling of turbochargers under hot and pulsating flow conditions at the turbine inlet. SAE Technical Papers, SAE Int 2014. https://doi.org/10.4271/2014-01-1080.
[27] Torregrosa A, García-Cuevas LM, Inhestern LB, Soler P. Radial turbine sound and noise characterisation with acoustic transfer matrices by means of fast one-dimensional models. Int J Engine Res 2021;22(4):1312–28. https://doi.org/10.1177/1468087419889429.
[28] Veloso R, Elnemr Y, Reich FM, Allam S. Simulation of sound transmission through automotive turbochargers. SAE Technical Papers, SAE Int 2012. https://doi.org/10.4271/2012-01-1560.
[29] De Bellis V, Marelli S, Bozza F, Capobianco M. 1D simulation and experimental analysis of a turbocharger turbine for automotive engines under steady and unsteady flow conditions. Energy Procedia 2014:909–18. https://doi.org/10.1016/j.egypro.2014.01.096. Elsevier Ltd.
[30] Kinsler LE, Frey AR, Coppens AB, Sanders JV. Fundamentals of acoustics. 4th ed. Wiley; 2000.
[31] Tiikoja H, Auriemma F, Lavrentjev J. Damping of acoustic waves in straight ducts and turbulent flow conditions. SAE Technical Papers, SAE Int 2016. https://doi.org/10.4271/2016-01-1816.
[32] Doehring D, Christmann L, Schlottke-Lakemper M, Gassner GJ, Torrilhon M. Fourth-order paired-explicit Runge-Kutta methods. Comput Sci Eng 2025;2(1):1. https://doi.org/10.1007/s44207-025-00005-4.
[33] Elnemr Y. Acoustic modeling and testing of exhaust and intake system components. Stockholm: KTH; 2011.
[34] Hirschberg A, Hoeijmakers M. Comments on the low frequency radiation impedance of a duct exhausting a hot gas, J Acoust Soc Am. vol. 136, no. 2, pp. EL84–EL89, Aug. 2014, doi: 10.1121/1.4885540.
[35] International Organization for Standardization, "Acoustics—Preferred reference values for acoustical and vibratory levels," Geneva, 2015.
[36] Rienstra SW. Fundamentals of duct acoustics. Brussels 2015.
[37] International Electrotechnical Commission, Electroacoustics—Octave-band and fractional-octave-band filters - Part 1: Specifications, IEC 61260-1:2014, Geneva., 2014. [Online]. Available: https://webstore.iec.ch/en/publication/5063.
[38] Joint Committee for Guides in Metrology, "Evaluation of measurement data - Guide to the expression of uncertainty in measurement," BIPM, Sèvres, JCGM 100:2008, 2008. doi: 10.59161/JCGM100-2008E.
[39] Heywood JB. Internal combustion engine fundamentals. 2nd ed. New York: McGraw-Hill Book Company; 2018.
[40] Hautala S, Mikulski M, Söderäng E, Storm X, Niemi S. Toward a digital twin of a mid-speed marine engine: from detailed 1D engine model to real-time implementation on a target platform. Int J Engine Res 2023;24(12):4553–71. https://doi.org/10.1177/14680874221106168.
[41] Bergman DR. Computational acoustics: theory and implementation. 1st ed. Hoboken, NJ: Wiley; 2018. 10.1002/9781119277323.
[42] Benzakein MJ, Zwick JW. Sound transmission and suppression in turbomachinery ducts, 1970. [Online]. Available: http://asmedigitalcollection.asme.org/GT/proceedings-pdf/GT1970/79856/V01AT01A058/2390078/v01at01a058-70-gt-58.pdf.
[43] Zhang S, Pang J, Zhang H, Yang L, Qing W. Phenomenon and analysis of low-frequency standing wave inside exhaust system. Lecture Notes Electr Eng 2015:325–34. https://doi.org/10.1007/978-3-662-45043-7_34. Springer Verlag.